Dalton Transactions

ROYAL SOCIETY OF CHEMISTRY

PAPER

View Article Online
View Journal | View Issue

Cite this: *Dalton Trans.*, 2025, **54**, 5075

Homoleptic coordination polymers and complexes of transition metals with 2-(1,2,4-1*H*-triazol-3-yl) pyridine and tuning towards white-light emission†

Marcel T. Seuffert,[a] Alexander E. Sedykh,[a] Thomas C. Schäfer,[a] Jonathan Becker[a] and Klaus Müller-Buschbaum *[a,b]

Twelve coordination compounds ranging from polymers to complexes based on divalent ions of the 3d-transition metals Mn to Zn, and Cd together with the ligand 2-(1,2,4-1*H*-triazol-3-yl)pyridine (Hpt) were synthesised and fully characterised. The main products are homoleptic, one-dimensional coordination polymers $^1_\infty$[M(pt)$_2$] (M = Mn–Zn, and Cd, pt = 3-(pyridin-2-yl)-1,2,4-triazolate), $^1_\infty$[Cu(pt)$_2$]·0.5Py, besides complexes [MX$_2$(Hpt)$_2$] from MnCl$_2$, FeCl$_2$, CoCl$_2$, CoBr$_2$, ZnCl$_2$, and Hpt = 2-(1,2,4-1*H*-triazol-3-yl)pyridine. In addition to these series, single crystalline by-products of the reactions were identified and their structures determined. The obtained products were investigated with single-crystal (SCXRD) and powder X-ray diffraction (PXRD), including temperature-dependent PXRD, physisorption experiments, UV-Vis, IR, and photoluminescence spectroscopy (PL), simultaneous thermal analysis, and elemental analysis. Based on $^1_\infty$[Zn(pt)$_2$], it was possible to generate a white light-emitting compound by addition of Eu^{3+} and Tb^{3+}. It follows the RGB concept with blue ligand-based emission of the coordination polymer and red/green emission of lanthanide ions and shows excitation dependent tuneable character of emission colour from blue to practically perfect white.

Received 11th November 2024,
Accepted 17th February 2025

DOI: 10.1039/d4dt03149k

rsc.li/dalton

Introduction

Coordination compounds and complexes have been under extensive chemical investigation and have multiple applications *e.g.*, functioning as catalysts[1] as well as for medical and biochemical purposes.[2] This includes *e.g.*, various zinc-based coordination compounds acting as anticancer agents,[3] or complexes based on the tridentate Schiff base ligand, 4-(2-((1*E*,2*E*)-1-(2-(*p*-tolyl)hydrazineylidene)-propan-2-ylidene)-hydrazineeyl) with anticancer or antimicrobial activities depending on contained metals.[4] Complexes of Fe(III), and Co(II) with Isatin-hydrazone derivates were reported showing anti-inflammatory properties.[5] Besides, coordination complexes can be utilised as sensor materials for various analytes by luminescence monitoring. For example, the formation of a complex and thereon fluorescence quenching of a 2-pyridinecarbonyl substituted 8-aminoquinoline derivative was reported being applicable to quantify Cu^{2+} in water and food.[6] A complex based on Pd(II) and a hydrazone derived Schiff base was found to be capable of ratiometric detection of F^-.[7] The compound [(ppy)$_2$Ir(IPP)]PF$_6$ (ppy = 2-phenylpyridine, IPP = 1-(1*H*-imidazo[4,5-*f*][1,10]phenatrolin-2-yl)phenol) was reported being applicable as a "*turn-off*" fluorescence sensor for Ni^{2+}.[8] This shows the numerous potential applications, coordination complexes possess.

By usage of multidentate ligands and depending on the ligand structure, it is possible to obtain polymeric coordination compounds, namely coordination polymers (CPs) and metal–organic frameworks (MOFs). These groups of coordination compounds were intensively studied over the recent years.[9–12,13] The properties of CPs and MOFs depend on their structure and containing building blocks – often metal ions and ligands – leading to various possible applications, such as electrochemical properties[14] resulting in energy storage implementations,[11,15] catalytic utilisation,[16,17] medical purposes,[9,12,18,19] and environmental protection applications.[10,16,20]

One of the most fascinating properties of manifold MOFs is photoluminescence, leading to applications like sensing,[21] bioimaging,[9,18,22] optoelectronic devices,[23] and aesthetical or anti-counterfeiting applications.[24,25] Investigated photoluminescent coordination compounds often contain multiple

[a]*Institute of Inorganic and Analytical Chemistry, Justus Liebig University Giessen, Heinrich-Buff-Ring 17, 35392 Giessen, Germany. E-mail: kmbac@uni-giessen.de*
[b]*Center for Materials Research (LAMA), Justus Liebig University Giessen, Heinrich-Buff-Ring 16, 35392 Giessen, Germany*

†Electronic supplementary information (ESI) available: Analytical methods as well as 50 figures and 39 tables showing the crystallographic data, powder X-ray diffractograms, photoluminescence spectra, luminescence intensity decays and corresponding lifetimes, absorption spectra, IR spectra, thermal properties, and physisorption properties. CCDC 2347927, 2347920, 2347949, 2347948, 2347938, 2347937, 2347952, 2347953, 2347947, 2347946, 2347951, 2347925, 2347917 and 2347950. For ESI and crystallographic data in CIF or other electronic format see DOI: https://doi.org/10.1039/d4dt03149k

chromophores, leading to the possibility of tuning the emission colour. This can be achieved *e.g.*, by functionalisation of MOFs with lanthanide ions.[26,27,28–31] White light emission is a frequently desired property of alike compounds, attained by utilising additive colour mixing according to the RGB concept.[25,28,32] Thereby, white light emitting CPs and MOFs as solid-state light sources are a more environment-friendly alternative to *e.g.* mercury containing fluorescent lights.[33,34] This makes them promising candidates for lighting technologies or anti-counterfeiting applications.[35] As a matrix material for such luminescent compounds, transition metal coordination polymers can be exploited, as it was shown for ZIF-8,[29,31] MOF-5,[26] or $^{3}_{\infty}\{[Zn_3(bdc)_3(EtOH)_2]\cdot(EtOH)_{0.6}\}$ (bdc = benzene dicaboxylate).[30] Moreover, by intercalation of Eu^{3+} and Tb^{3+} to MIL-124, a white light emitter was created, which potentially can be utilised in luminescent devices like displays, or for lighting.[33] Furthermore, a coordination polymer gel obtained by reaction of europium acetate and terbium acetate with 5,5′,5″-((benzene-1,3,5-tricarbonyl)tris(azanedi-yl))triisophthalic acid featuring white light emission was published, which is applicable as invisible anti-counterfeit ink.[36] By coating of UV-LEDs with a composite comprising carbon dots, and the MOF $[Eu_{1.22}Tb_{0.78}(1,4\text{-phda})_3(H_2O)](H_2O)$ it was possible to generate a white LED.[37]

There are several examples of CPs containing transition metals and 1,2,4-1*H*-triazole (TzH), or rather 1,2,4-triazolate (Tz), as ligand.[38] It was shown, that those compounds can exhibit guest-sensitive luminescence.[39] Therefore, also derivates of triazoles are of increasing scientific interest as potential ligands for CPs with photoluminescent properties. A ligand, which was recently used for this purpose, is 2-(1,2,4-1*H*-triazol-3-yl)pyridine (Hpt)[40–42,43–47] or derivates of it.[46,48,49] Numerous compounds based on these ligands in combination with transition metals were reported, such as coordination polymers, like the isotypic, homoleptic compounds $^{1}_{\infty}[Ni(pt)_2]\cdot 1.5H_2O$ [40] and $^{1}_{\infty}[Cu(pt)_2]\cdot H_2O$,[41] as well as the heteroleptic polymers $^{1}_{\infty}[Cu_2I(pt)_2]$,[50] and $^{1}_{\infty}[Cu(pt)(OAc)]$.[51] They all exhibit a one-dimensional polymeric structure with η^2-μ_2-coordination mode of the deprotonated pt ligand. Also, compounds containing derivates of Hpt were published, such as $^{3}_{\infty}[Cu(H\text{-}2py\text{-}trz\text{-}pba)_2]$ (H-2py-trz-*p*ba = 4-(3-(Pyridin-2-yl)-4*H*-1,2,4-triazol-4-yl)benzoate),[52] $[Mn_2(bpt)_2(SCN)_2(H_2O)_2]$ (containing the Hpt derivate bpt = 3,5-bis(2-pyridyl)-4*H*-1,2,4-triazole),[46] and $^{1}_{\infty}[Zn(5\text{-nipa})(L^{22})(H_2O)]$ (5-nipa = 5-nitroisophthalate, L^{22} = 2,2′-(4*H*-1,2,4-triazole-3,4-diyl)dipyridine).[49]

Various reported compounds also feature additional properties, like $[Fe(Hpt)_3](BF_4)_2\cdot H_2O$, which shows a temperature-dependent spin crossover of Fe(II).[43] Also, the d^{10} transition metal ion Cu(I) forms complexes with Hpt derivates, such as $[Cu(bptzH)(PPh_3)_2](ClO_4)$ (bptzH = 2-(3-*tert*-butyl-1,2,4-1*H*-triazol-5-yl)pyridine), $[Cu(fptzH)(PPh_3)_2](ClO_4)$ (fptzH = 2-(3-trifluoromethyl-1,2,4-1*H*-triazol-5-yl)pyridine), and $[Cu(bptzH)(dppe)](ClO_4)$ (dppe = 1,2-bi(diphenylphosphino)ethane), which all show intense, luminescence in the solid state with emission colours from blue to green.[53] This shows the potential of coordination compounds based on Hpt and its derivates with regard to optical properties.

In this work, we extend the number of coordination compounds based on Hpt and present the structures and properties of new compounds with 3-(pyridin-2-yl)-1,2,4-triazolate (pt) as ligand, namely the polymers $^{1}_{\infty}[M(pt)_2]$ (M = Mn (**1**), Fe (**2**), Co (**3**), Ni (**4**), Cu (**5**), Zn (**6**), Cd (**7**)), and $^{1}_{\infty}[Cu(pt)_2]\cdot 0.5Py$ (**8**), besides the complexes $[MX_2(Hpt)_2]$ (MX_2 = $MnCl_2$ (**9**), $FeCl_2$ (**10**), $CoCl_2$ (**11**), $CoBr_2$ (**12**)) containing 2-(1,2,4-1*H*-triazol-3-yl) pyridine (Hpt). Depending on the contained transition metal ion, the synthesised CPs can exhibit photophysical properties and – in case of a zinc-containing CP – can even be used as blue component of a RGB-type white light-emitter.

The obtained compounds were investigated with regard to structure, photophysical properties and thermal properties, which is described hereafter.

Results and discussion

The compounds $^{1}_{\infty}[Zn(pt)_2]$ (**6**), $^{1}_{\infty}[Cu(pt)_2]\cdot 0.5Py$ (**8**), $[MnCl_2(Hpt)_2]$ (**9**), $[FeCl_2(Hpt)_2]$ (**10**), $[CoCl_2(Hpt)_2]$ (**11**), $[CoBr_2(Hpt)_2]$ (**12**), and $[ZnCl_2(Hpt)_2]$ (**13**) were obtained as single crystals suitable for SCXRD. Therefore, the crystal structures were determined for these compounds based on SCXRD data, isostructural or even isotypic character of further elements of the series of compounds were determined by PXRD.

Syntheses of and crystal structure investigations on $^{1}_{\infty}[M(pt)_2]$ (1–7)

Based on single crystal X-ray data, the crystal structure of this series of compounds was determined for the homoleptic, one-dimensional coordination polymer (CP) $^{1}_{\infty}[Zn(pt)_2]$ (**6**). Crystals of **6** suitable for single crystal X-ray diffraction investigations were obtained by reaction of water-free $ZnCl_2$, 2-(1,2,4-1*H*-triazol-3-yl)pyridine (Hpt), and benzylamine in a mixture of toluene and pyridine. CP **6** crystallises in the tetragonal crystal system in the space group $I4_1/acd$. The CP contains distorted, zinc-based octahedra, in which Zn^{2+} is coordinated by four deprotonated, 3-(pyridin-2-yl)-1,2,4-triazolate (pt) ligand molecules. Two η^2-pt ligands coordinate *via* N1 of the pyridine ring and N2 of the triazole ring. The other two η^1 ligand molecules coordinate *via* N3 of the triazole ring to Zn. Thereby, each pt ligand coordinates to two zinc ions. This results in octahedra which are interconnected by two neighbouring nitrogen atoms of the triazole rings (here N2 and N3). The consequential, one-dimensional polymeric strands screw about the crystallographic *c* axis and are stacked within the unit cell, forming square-shaped pore channels.

Detailed crystallographic data is listed in Table S1.† A depiction of the crystal structure is given in Fig. 1. Considering weak C–H···N interactions,[54] each pt ligand establishes two hydrogen bonds to ligand molecules of a neighbouring polymeric strand. This results in a supermolecular three-dimensional polymeric structure (Fig. S1†).

The interatomic Zn–N distances in CP **6** were determined to be within the range of 207(5) pm to 232(4) pm (Table S2†). These distances match with published values for *e.g.* $^{3}_{\infty}[Zn(H\text{-}2py\text{-}trz\text{-}ia)]\cdot 5.25H_2O$ (H-2py-trz-ia = 5-(3-pyridyl-1,2,4-triazol-

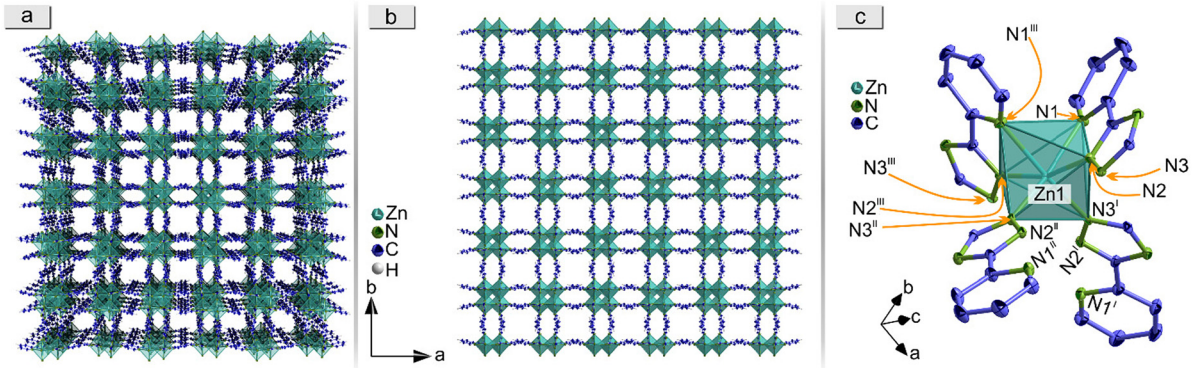

Fig. 1 Depiction of the crystal structure of $^1_\infty$[Zn(pt)$_2$] (**6**). Presented are: A three-dimensional depiction of the square-shaped pore channels along the crystallographic *c* axis (a), an excerpt of the crystal structure along the crystallographic *c* axis in parallel projection (b), and the extended coordination of Zn^{2+} (c, hydrogen atoms are omitted). Polyhedra around Zn are highlighted dark cyan. Displayed thermal ellipsoids correspond to 50% probability level of the atoms. For clarity, only one of the two disorders of the ligand molecule is depicted. Crystallographic data is summarised in Table S1.† Symmetry operations: I = 1/4 + *y*, 1/4 − *x*, −1/4 + *z*; II = *x*, −*y*, 1/2 − *z*; III = 1/4 − *y*, 1/4 − *x*, 1/4 − *z*.

4-yl)iso-phthalate), which contains fivefold coordinated Zn^{2+} interconnected three-dimensionally by H-2py-z-ia, and for which corresponding distances in a range of 212–221 pm are reported.[47]

The distances in **6** are also in good agreement with distances in $^1_\infty$[Zn(5-nipa)(L^{22})(H_2O)] (5-nipa = 5-nitro-isophthalate, L^{22} = 2,2′-(4*H*-1,2,4-triazole-3,4-diyl)dipyridine),[49] which contains octahedrally coordinated Zn^{2+} and for which Zn–N distances of 214–235 pm are reported.

By comparison of the reported sum formulas, CP **6** is closely related to reported compounds $^1_\infty$[Ni(pt)$_2$]·1.5H_2O,[40] and $^1_\infty$[Cu(pt)$_2$]·H_2O,[41] which also feature octahedral coordination of the metal ions by η^2-μ_2-coordinating pt ligands and one-dimensional polymeric structures. Within these two CPs, polymeric zig-zag chains with two different orientations within the unit cell are formed, rather than screwing strands as observed for **6**. This leads to a denser packing within the unit cell for the already reported compounds in comparison to **6**. For the single crystal structure of CP **6**, a residual electron density of 215 electrons per unit cell located in the square-shaped channels were found, indicating solvent molecules being intercalated there.

PXRD investigations on $^1_\infty$[M(pt)$_2$]

Bulk materials of $^1_\infty$[M(pt)$_2$] (**1–7**) were obtained by solvothermally reacting stoichiometric amounts of the metal acetate (hydrates) M(OAc)$_2$·*x*H_2O, M = Mn–Zn, Cd, and the ligand Hpt in pyridine (see Experimental section). Subsequent to washing with fresh solvent and drying in vacuum, the homoleptic compounds $^1_\infty$[M(pt)$_2$] (M = Mn (**1**), Fe (**2**), Co (**3**), Ni (**4**), Cu (**5**), Zn (**6**), Cd (**7**)) are obtained, which are isotypic, and can be synthesised phase-pure, as proven by powder diffractograms (Fig. 2). The isotypic character of the CPs **1–7** was confirmed by Pawley refinements (see Fig. S4, and Table S15†). By these, the cell constants of **1–7** were determined to the values listed in Table S27.†

It is noteworthy, that CP **5** ($^1_\infty$[Cu(pt)$_2$]) differs from the already reported compound $^1_\infty$[Cu(pt)$_2$]·H_2O[41] although having

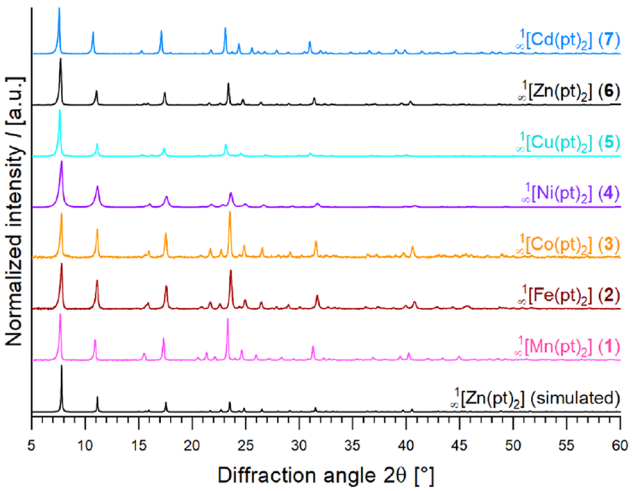

Fig. 2 PXRD patterns of $^1_\infty$[M(pt)$_2$] (M = Mn (**1**), Fe (**2**), Co (**3**), Ni (**4**), Cu (**5**), Zn (**6**), Cd (**7**)), in comparison to a pattern of **6** simulated from SCXRD data.

the same polymer sum formula. Indeed, **5** is isotypic to $^1_\infty$[Zn(pt)$_2$] (**6**) as proven by PXRD and Pawley refinement utilizing SCXRD data of **6** (see Fig. 2, Fig. S4, and Table S15†). Hence, **5** also crystallises in the tetragonal crystal system in a body-centred Bravais lattice and exhibits polymeric strands screwing about crystallographic *c* axis, as described above. Contrary, $^1_\infty$[Cu(pt)$_2$]·H_2O [41] contains polymeric zig-zag chains with two different orientations within the unit cell crystallizing in a primitive Bravais lattice.[41]

Temperature-dependent PXRD investigations on $^1_\infty$[M(pt)$_2$]

The effect of intercalated solvents is further noticeable. Differences in reflection intensities between recorded patterns and the simulated pattern of $^1_\infty$[Zn(pt)$_2$] (**6**), which are observable within Fig. 2, can be explained by solvent molecules being intercalated within the square-shaped pore channels. An influ-

ence on reflection intensities is a known effect of guests being present in pore systems.[55] Furthermore, different constituting metal ions and the tendency of these CPs to crystallise with a needle-shaped habitus leading to preferred orientation effects with regard to PXRD influence the reflection intensities, as well.

To investigate the differences and changes of reflection intensities more intensively, temperature-dependent PXRD recordings were performed. When analysing respective patterns of $^1_\infty$[Zn(pt)$_2$] (**6**) (Fig. 3), the intensity of the (2 0 0) reflection at approx. 7.8° in 2θ shows the largest detectable variation in intensity in dependence of temperature T and increases upon heating (between 30 °C and 405 °C). Since related lattice planes intersect the square-shaped pore channels (Fig. 4), the intensity of this reflection is possibly influenced by guest molecules intercalated in the pores. With increasing temperature, the differences in intensities between recorded and simulated patterns of **6** diminish with solvent molecules leaving the pores. The powder pattern of **6** can be identified up to a temperature of 430 °C, while the intensities of observed reflections start to decrease above 405 °C, as shown for the four most intense reflections in Fig. S6.† Additionally, the broad reflections that are assigned to the formation of $ZnCN_2$, begin to emerge. At 455 °C, the coordination polymer is decomposed completely, and the majority phase is identified as $ZnCN_2$ (Fig. 3).

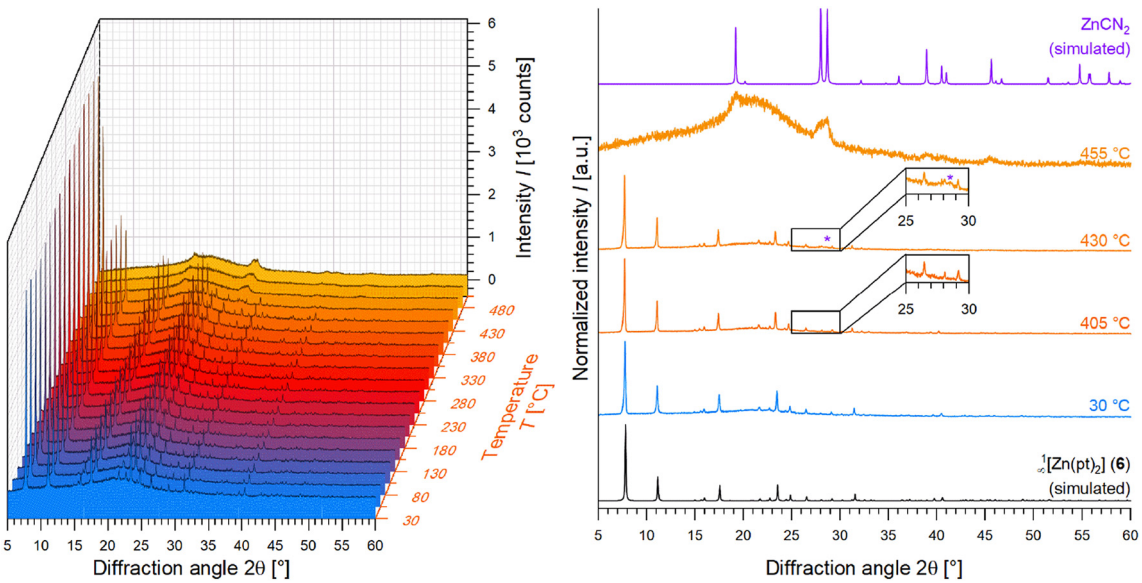

Fig. 3 Temperature-dependent powder X-ray diffractograms of $^1_\infty$[Zn(pt)$_2$] (**6**) reaching from 30 °C to 505 °C in steps of 25 °C (left) besides recorded diffractograms of **6** at 30 °C, 405 °C and 430 °C in comparison to diffractograms CP **6**, and $ZnCN_2$,[61] both simulated from respective SCXRD data (right).

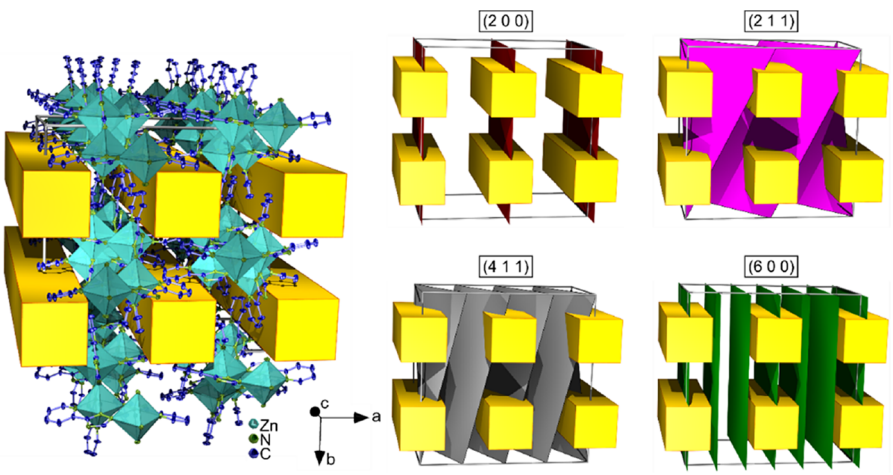

Fig. 4 3D depiction of the crystal structure of $^1_\infty$[Zn(pt)$_2$] (**6**) with square-shaped pore channels marked as yellow cuboids, as well as 3D depictions of the unit cell without atoms and inserted lattice planes. Lattice planes corresponding to the most intense PXRD reflections observed are inserted as coloured planes: red = (200), pink = (211), grey = (411), green = (600).

Analogous temperature-dependent PXRD investigations were performed for $^1_\infty$[M(pt)$_2$] (M = Mn (**1**), Fe (**2**), Co (**3**), Ni (**4**), Cu (**5**), Cd (**7**)) leading to comparable results.

For $^1_\infty$[Mn(pt)$_2$] (**1**), the formation of unknown phase(s) is observable. $^1_\infty$[Fe(pt)$_2$] (**2**) converts to a high pressure phase of magnetite,[56] followed by transition to magnetite[57] at 480 °C and finally to hematite[58] at 505 °C. $^1_\infty$[Co(pt)$_2$] (**3**) and $^1_\infty$[Cu(pt)$_2$] (**5**) decompose to amorphous compounds. Temperature-dependent PXRD investigations on $^1_\infty$[Ni(pt)$_2$] (**4**) show the formation of Ni_3C [59] above 280 °C. In analogy to the high-temperature behaviour of $^1_\infty$[Zn(pt)$_2$] (**6**) described above, CP **7** ($^1_\infty$[Cd(pt)$_2$]) decomposes to $CdCN_2$ [48] above 405 °C, at first, which subsequently converts to CdO [60] at 505 °C. Temperature-dependent PXRD investigation results are summarised in Table 1. Corresponding PXRD patterns are given within the ESI (Fig. S6–S18†), besides Fig. 3. This shows that the solvents can be removed from square-shaped pore channels by thermal treatment.

Table 1 Sum formula and temperature, up to which the compound is stable (T_{st}), the compound is identifiable by PXRD (T_{max}), temperature, at which reflections of the coordination polymer are no longer observable by PXRD (T_{dec}), as well as the resulting majority phase

Compound	Sum formula	T_{st} [a] [°C]	T_{max} [°C]	T_{dec} [°C]	Majority phase at T_{dec}
1	$^1_\infty$[Mn(pt)$_2$] [b]	330	430	455	Unknown phase
2	$^1_\infty$[Fe(pt)$_2$] [b]	305	430	455	Fe_3O_4 (magnetite [d])[56]
3	$^1_\infty$[Co(pt)$_2$] [b]	455	455	480	Amorphous
4	$^1_\infty$[Ni(pt)$_2$] [b]	280	480	505	Ni_3C [59]
5	$^1_\infty$[Cu(pt)$_2$] [b]	305	330	330	Amorphous
6	$^1_\infty$[Zn(pt)$_2$] [c]	405	430	455	$ZnCN_2$ [61]
7	$^1_\infty$[Cd(pt)$_2$] [b]	405	430	455	$CdCN_2$ [e62]

[a] The temperature stability was evaluated by investigation of reflection intensities in temperature-dependent PXRD. As soon as a drop in intensity of the reflections is observed, the beginning decomposition of the crystalline structure is assumed. [b] See also Fig. S7–S18.† [c] See Fig. 3, and Fig. S6.† [d] High-pressure crystal structure of magnetite at 250 kPa. It converts to magnetite[57] at 455 °C and finally to hematite[58] at 505 °C. [e] Transition to CdO [60] is observed at 505 °C.

Crystal structure of the one-dimensional, homoleptic coordination polymer $^1_\infty$[Cu(pt)$_2$]·0.5Py (**8**)

A structure which is closely related to CP **6**, was found for the coordination polymer $^1_\infty$[Cu(pt)$_2$]·0.5Py (**8**, Fig. 5). This compound crystallises in the orthorhombic crystal system in the space group *Ibca*. The same structural motif of $^1_\infty$[Zn(pt)$_2$] (**6**) is present in CP **8**. It contains distorted, copper-ion-based octahedra, in which Cu^{2+} is coordinated by four deprotonated pt molecules, two η^2- and two η^1-pt, in analogy to CP **6**.

Solvent molecules (pyridine) are intercalated in the rectangular pore channels in a *crystallographically ordered* manner, resulting in a change of the crystal system from tetragonal to orthorhombic in comparison to $^1_\infty$[Zn(pt)$_2$] (**6**).

Excerpts of the crystal structure of CP **8** are given in Fig. 5 and Fig. S2.† Detailed crystallographic information is given in Table S3.† Interatomic Cu–N distances ranging from 198(3) pm to 260(2) pm (Table S4†) coincide with distances reported for the one-dimensional coordination polymer $^1_\infty$[Cu(pt)$_2$]·H_2O, which consist of pt-linked, Cu(II)-based octahedra. Interatomic Cu–N distances for this compound are ranging from 197 pm to 254 pm.[41]

PXRD investigations on $^1_\infty$[Cu(pt)$_2$]·0.5Py (**8**)

As mentioned above, the CPs $^1_\infty$[M(pt)$_2$] can be obtained as bulk material by solvothermal reaction of metal acetates and Hpt in pyridine. However, due to the porosity of these substances, solvent molecules are intercalated. Accordingly, drying is essential to achieve $^1_\infty$[Cu(pt)$_2$] (**5**). The product initially obtained by reaction of Cu(OAc)$_2$·H_2O and Hpt in pyridine (without washing and vacuum drying), contained both, single crystals of $^1_\infty$[Cu(pt)$_2$]·0.5Py (**8**) and reflections of **8** in the powder diffractogram, only. This means, the as-synthesised, still damp product of the reaction of Cu(OAc)$_2$·H_2O and Hpt

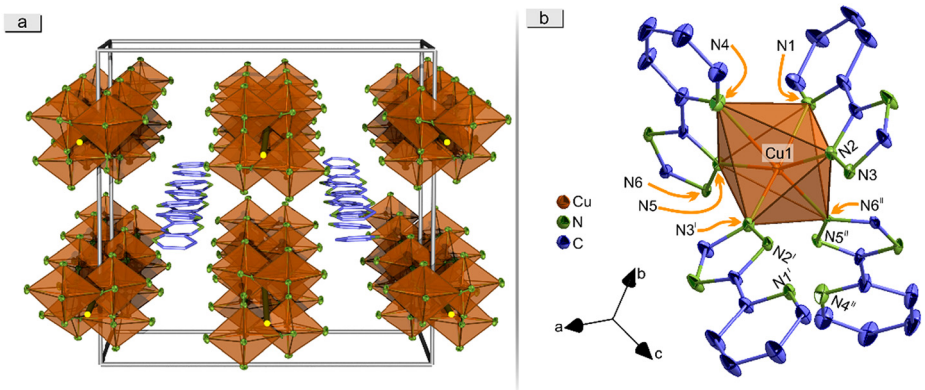

Fig. 5 Depiction of the crystal structure of $^1_\infty$[Cu(pt)$_2$]·0.5Py (**8**). Presented are: An enlarged 3D illustration of the rectangular channels within the elemental cell with depiction of both disorders of trapped pyridine molecules (a; for simplification, only Cu atoms and coordinating N atoms of the CP are depicted and pyridine molecules are shown in wire stick representation), as well as the extended coordination of Cu^{2+} (b; hydrogen atoms are omitted). Polyhedra around Cu are highlighted in orange. Displayed thermal ellipsoids correspond to 50% probability level of the atoms. Crystallographic data is summarised in Table S3.† Symmetry operations: I = 1 – *x*, 3/2 – *y*, *z*; II = 3/2 – *x*, *y*, 1 – *z*.

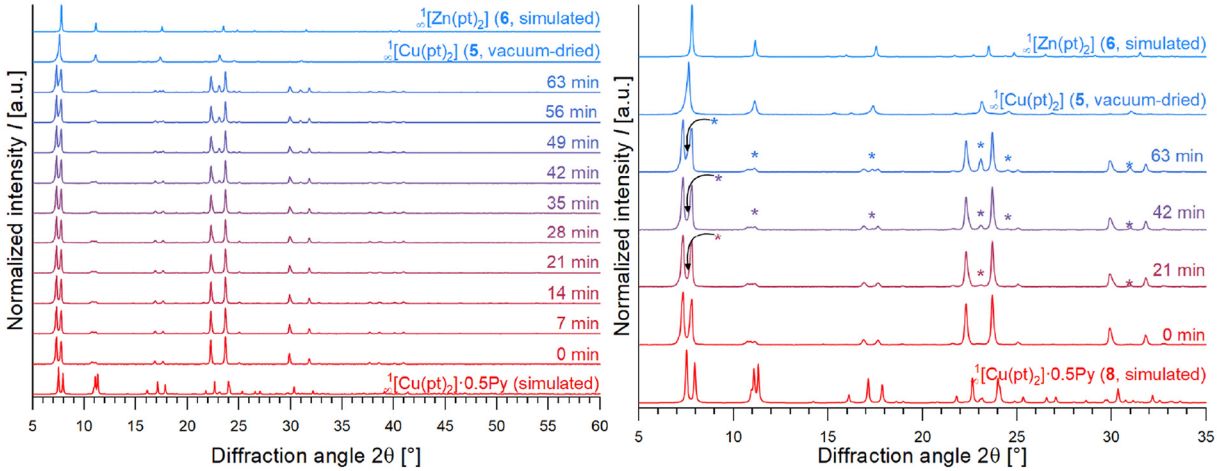

Fig. 6 Powder X-ray diffractograms of the reaction product of $Cu(OAc)_2{\cdot}H_2O$ and Hpt in pyridine after air-drying for given durations as well as a pattern of the vacuum-dried product in comparison to patterns of $^1_\infty$[Cu(pt)$_2$]·0.5Py (CP **8**) and $^1_\infty$[Zn(pt)$_2$] (CP **6**), both simulated from respective SCXRD data. Upon air-drying, the reflections of CP **5** appear. After vacuum-drying, the pattern of the product shows reflections of **5**, only.

contains $^1_\infty$[Cu(pt)$_2$]·0.5Py (**8**) as majority phase instead of **5**. However, CP **8** is only stable in the presence of pyridine and converts completely into $^1_\infty$[Cu(pt)$_2$] (**5**) upon drying, which was proven by comparison of recorded PXRD patterns after several minutes of air-drying and complete vacuum-drying (Fig. 6, reflections corresponding to **5** are marked with*). The pattern of a freshly synthesised, still damp product shows reflections of CP **8**, only. Upon drying, the reflections of CP **5** begin to appear. The vacuum-dried product exhibits reflections of **5**, only (Fig. 6). This shows the direct effect of crystallographically ordered solvent molecules within the structure, leading to the reduction of the symmetry as described above.

Photophysical properties of selected compounds

Photoluminescence properties of impregnated $^1_\infty$[Zn(pt)$_2$]. Due to constituting metal atoms, the synthesised compounds feature conspicuous optical properties, like intense colour for compounds containing ions of iron, cobalt, nickel, or copper. The coordination polymers $^1_\infty$[M(pt)$_2$] (M = Mn (**1**), Zn (**6**)) are colourless (determined according to *L*a*b** scatter diagrams, see Fig. 7, Fig. S20 and Table S16†).

Considering potential luminescence application, these two candidates are therefore appropriate due to their white appearance and, hence, low absorption of visible light. Upon UV excitation, **6** exhibits blue luminescence. Since both, incoming UV and emitted light, are not absorbed by Zn^{2+} ion due to the d^{10} electron configuration, this emission is considered as ligand-based.

The pure ligand exhibits a broad band emission in the UV/blue region upon UV excitation ($\lambda_{em\ max}$ = 360 nm, λ_{exc} = 324 nm, Fig. S22, and S24†), while the emission band of CP **6** is located at $\lambda_{em\ max}$ = 337 nm for excitation at 306 and 311 nm. At higher excitation wavelengths (λ_{exc} = 324 nm; 346 nm) $\lambda_{em\ max}$ = 360 nm is located at 395 nm (Fig. S23 and S25†).

Comparable photoluminescence behaviour was reported for other d^{10} transition metal compounds, *e.g.* for

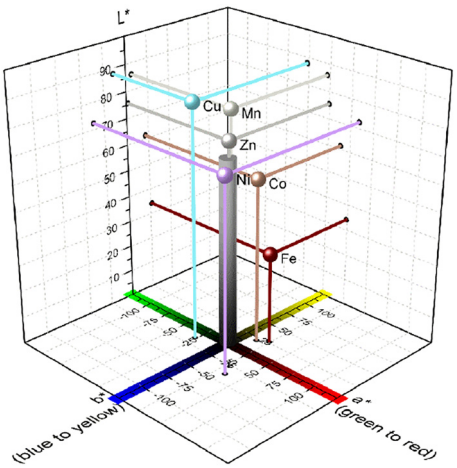

Fig. 7 *L*a*b** scatter diagram with inserted *L*a*b* chromaticity coordinates of the coordination polymers $^1_\infty$[M(pt)$_2$] (M = Mn (**1**), Fe (**2**), Co (**3**), Ni (**4**), Cu (**5**), Zn (**6**)). Corresponding reflectance spectra are given in Fig. S20.† Calculated chromaticity coordinates are listed in Table S16.†

$[Zn_6(H_2O)_3(dmf)_6(ur)_2(tdc)_6]{\cdot}4H_2O$ (ur = urotropin, tdc = 2,5-thiophenedicarboxylate), which exhibits a broad emission at 470 nm (λ_{exc} = 380 nm) assigned to intra-ligand $\pi^* \rightarrow \pi$ or LMCT transitions,[63] or $[Zn_3(btc)_2(tpt)(H_2O)_2]{\cdot}4H_2O$ (btc = 3,5-benzenetricarboxylate, tpt = tris(4-pyridyl)triazine) featuring a broad emission around 380 nm (λ_{exc} = 280 nm) assigned to the $\pi^* \rightarrow \pi$ transition of the N-donor ligand tpt.[64] Likewise, [Cu(bptzH)$(PPh_3)_2$](ClO_4), exhibits blue luminescence (λ_{em} = 456 nm) upon UV excitation.[53] The observed luminescence of the coordination polymer (see lifetime determination following) is therefore considered ligand based and may be explained with $\pi^* \rightarrow \pi$ of higher energy levels (compared to pure ligand Hpt) of the deprotonated ligand pt^- and/or LMCT.[63,65]

The photoluminescence properties render $^{1}_{\infty}[Zn(pt)_2]$ a suitable candidate to function as the blue component of an RGB-type white light emitter. To generate a suchlike luminescent compound, an impregnation of the square-shaped pore channels of CP **6** with Eu^{3+} ions as red emitter, and Tb^{3+} ions as green emitter, was performed. For this purpose, an activated sample of CP **6** was dispersed and stirred in a solution containing equal amounts of $Eu(NO_3)_3{\cdot}6H_2O$ and $Tb(NO_3)_3{\cdot}6H_2O$ for eight days followed by centrifugation, decantation and vacuum drying of the solid product.

Three different solvents, namely *N*,*N*-dimethylformamide (DMF), acetonitrile (MeCN), and methanol (MeOH), were evaluated (For detailed information, see Experimental section.). Exemplarily, emission and excitation spectra, besides the chromaticity diagram of the product of impregnation in DMF – which is hereafter to be referred to as $EuTb@^{1}_{\infty}[Zn(pt)_2]$ – are shown in Fig. 8, and Fig. 9, respectively.

For excitation at λ_{exc} = 306 nm, 311 nm, and 324 nm, the emission spectra feature broad bands in the UV/blue region at wavelengths of 337 nm and 424 nm. Besides these, characteristic 4f–4f-transitions of the two lanthanide ions, Eu^{3+} and Tb^{3+}, are detected. As shown by the excitation spectra, the emission at 337 nm is initiated by excitation at 311 nm. The excitation spectrum for the emission band at λ_{em} = 424 nm features a maximum at λ_{exc} = 306 nm with a shoulder at 324 nm. The excitation spectra of most intense transitions of Tb^{3+} (544 nm) and Eu^{3} (617 nm) exhibit a maximum at λ_{exc} = 324 nm with a shoulder at 346 nm. A comparison between the emission spectra of pure Hpt, $^{1}_{\infty}[Zn(pt)_2]$ (**6**), and $EuTb@^{1}_{\infty}[Zn(pt)_2]$ (Fig. S26†) shows, that the blue luminescence of $EuTb@^{1}_{\infty}[Zn(pt)_2]$ corresponds to the luminescence observed for CP **6**.

However, the observed band at 424 nm for λ_{exc} = 306, 311, and 324 nm is not present within emission spectra of non-impregnated, pure $^{1}_{\infty}[Zn(pt)_2]$. This indicates a different source of this band. One possible explanation is, that this band arises due to formation of exciplexes between the lanthanide species inside the pore system and the coordination polymer. Interestingly, the emission band at 424 nm vanishes at λ_{exc} = 346 nm and a new emission band is observed at $\lambda_{em\ max}$ = 395 nm, which coincides with the spectrum for non-impregnated CP **6** at the same excitation wavelength. For short excitation wavelengths, the blue CP-based emission exceeds the lanthanide-based luminescence, wherefore the resulting overall emission colour is neon blue.

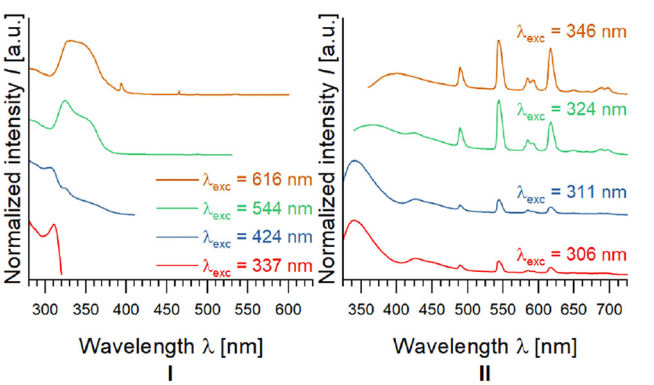

Fig. 8 Excitation (left) and emission spectra (right) of $^{1}_{\infty}[Zn(pt)_2]$ impregnated with Eu^{3+} and Tb^{3+} ions for eight days using DMF as solvent.

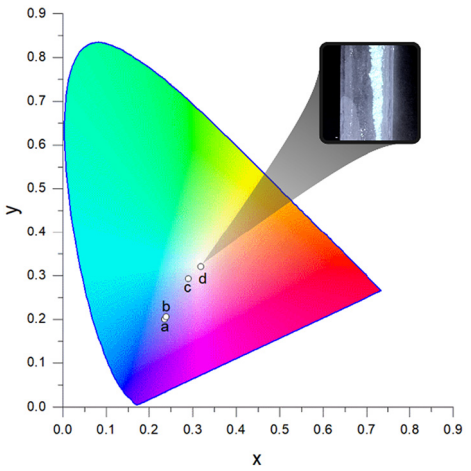

Fig. 9 CIE chromaticity diagram of $^{1}_{\infty}[Zn(pt)_2]$ (CP **6**) impregnated with Eu and Tb in DMF as solvent with inserted chromaticity coordinates *xy* at different excitation wavelengths. a: λ_{exc} = 306 nm, b: λ_{exc} = 311 nm, c: λ_{exc} = 324 nm, d: λ_{exc} = 346 nm. Accordingly, the lanthanide luminescence results from a sensitisation effect of the direct surrounding of the respective lanthanide ions, also known as *antenna effect*.[66–68]

With rising excitation wavelength, the lanthanide transitions become more dominant in the emission spectrum (Fig. 8) resulting in a shift of the chromaticity. Hence, a variation in intensity ratios of the observed bands in dependence of the excitation wavelength, was determined for $EuTb@^{1}_{\infty}[Zn(pt)_2]$ synthesised in DMF. This results in variable chromaticity (Fig. 8 and 9). In fact, the emitted light of $EuTb@^{1}_{\infty}[Zn(pt)_2]$ impregnated in DMF, when excited at λ_{exc} = 346 nm, exhibits chromaticity coordinates according to CIE of *xy* = (0.32|0.32). It therefore reaches practically perfect white chromaticity (*xy* = (0.333...|0.333...), Fig. 9). Thus, the concept of an excitation dependent red-shift of emission was utilised for an emission tuning towards RGB white light emission.

For the products of impregnations in methanol (Fig. S27†) and acetonitrile (Fig. S28†), qualitatively the same emission and excitation bands are observed, resulting in an analogous dependency of emission colour on excitation wavelength (Fig. S29, and S30†) Therefore, involved radiative processes are considered as independent from the chosen solvent.

As a result, the overall luminescence occurs due to excitation of the ligand followed by light emission of the CP (blue), as well as energy transfer to the lanthanides and subsequent characteristic Tb^{3+} (green) and Eu^{3+} (red) emissions. The respective solvent utilised for impregnation does not participate in the radiative luminescence processes. Corresponding chromaticities of the products from impregnation in acetonitrile and methanol at λ_{exc} = 346 nm are less ideal and given in Fig. S29 and S30.†

A comparison of scanning electron microscopy images before and after impregnation of **6** with Eu^{3+} and Tb^{3+}shows, that the habitus of CP **6** crystallites does not change upon impregnation (see Fig. S38†). Lanthanide contents between 1.7 and 2.3 wt% were determined by inductively coupled mass spectrometry (ICP-MS, for details, see Table S28†).

In summary, the coordination polymer $^1_\infty$[Zn(pt)$_2$] (**6**) being a blue light emitter, is capable of forming an RGB emitter by impregnation with Eu and Tb ions. Thereby, due to dependency of band intensities on excitation wavelength, the emission colour is tuneable from neon blue to white light (Fig. 9).

In addition to the qualitative photoluminescence characterisations, the luminescence lifetimes of the white light emitter EuTb@$^1_\infty$[Zn(pt)$_2$] were determined. For the emission band at λ_{em} = 395 nm excited at λ_{exc} = 340 nm of pure $^1_\infty$[Zn(pt)$_2$] (without lanthanide impregnation), the luminescence intensity decay can be described by a multi-exponential fit function leading to determination of the lifetimes τ_1 = 1.00(2) ns, and τ_2 = 3.10(3) ns. An average luminescence lifetime[69,70] of τ_{av} = 1.95 (3) ns was calculated. For the pure ligand, the lifetimes t_1 = 1.16 (1) ns, and t_2 = 2.89(3) resulting in τ_{av} = 1.58(2) ns were determined, which are of the same magnitude as lifetimes of pure CP **6** (For detailed description of the calculation, see ESI.†).

For EuTb@$^1_\infty$[Zn(pt)$_2$], τ_{av} for λ_{em} = 395 nm (λ_{exc} = 340 nm) was determined as 2.11(3) ns. Hence, the luminescence lifetime is slightly elongated for $^1_\infty$[Zn(pt)$_2$] (**6**) impregnated with lanthanides in comparison to non-impregnated CP **6**. This can be explained by rigidification due to coordination of pt to Zn^{2+}, which results in reduced vibrational freedom of the ligand and, hence, reduced rate of non-radiative depopulation of excited states[71] The recorded luminescence intensity decays of lanthanides within EuTb@$^1_\infty$[Zn(pt)$_2$] had to be fitted with a multi-exponential function, as well, in order to obtain a good quality of fit. Thereby, for Eu^{3+} emission (λ_{em} = 698 nm, λ_{exc} = 346 nm), two luminescence lifetimes were found (τ_1 = 0.48(3) ms, τ_2 = 1.30(3) ms), resulting in τ_{av} = 1.04(2) ms. In case of Tb^{3+} emission (λ_{em} = 544 nm, λ_{exc} = 346 nm), lifetimes of τ_1 = 0.40(2) ms and τ_2 = 1.160(6) ms were determined resulting in τ_{av} = 1.028(6) ms. These values in the µs–ms region all coincide with the range, in which lifetimes of the respective lanthanide ions are expected.[67,68,72] The discovery of two luminescence lifetimes for luminescent constituents indicates *e.g.* occupation of different positions within the pores resulting in varied chemical surroundings and, therefore, different non-radiative depopulation rates. In principle, the formation of lanthanide-containing side phases could also lead to detection of multiple luminescence lifetimes. However, PXRD patterns of EuTb@$^1_\infty$[Zn(pt)$_2$] impregnated in different solvents show reflections of the coordination polymer, only (Fig. S19†). Variations in reflection intensities further substantiate the assumption of lanthanide species intercalated in the pores of **6**.

An influence of the solvents utilised for impregnation on luminescence lifetimes by non-radiative processes can be assumed, as variations in τ_{av} are observed when using *e.g.* MeOH instead of DMF. For EuTb@$^1_\infty$[Zn(pt)$_2$] prepared in methanol, an average lifetime of the CP emission is determined to τ_{av} = 1.27(2) ns, which is 59% of the value for the composite prepared in DMF (2.14(2) ns). This can be explained by non-radiative depopulation processes involving the O–H group of methanol.[73] For Eu^{3+} (τ_{av} = 0.86(2) ms) and Tb^{3+} based emission (τ_{av} = 0.927(5) ms), the influence on lifetimes is less pronounced, resulting in the described overall changes of the chromaticity. All determined fitting parameters and calculated average luminescence lifetimes are summarised in Table S20.† Furthermore, the quantum yield was determined for the white light-emission of EuTb@$^1_\infty$[Zn(pt)$_2$] prepared in DMF. With an excitation wavelength of λ_{exc} = 346 nm, a quantum yield of 24(3) % was reached.

Absorption properties of $^1_\infty$[M(pt)$_2$]. As described above, distinct colour of some coordination polymers $^1_\infty$[M(pt)$_2$] (depending on contained metal atom) was observed (Fig. 10, Fig. S20 and Table S16†). Accordingly, the absorption properties were investigated in the solid state. For $^1_\infty$[Fe(pt)$_2$] (**2**), high absorbance at 250–300 nm, most likely occurring from π* ← π transitions of the ligand, was observed.

Furthermore, high absorbance in the blue/green region (overlapping bands at approx. 400 and 500 nm) caused most likely by MLCT was detected, leading to the blood-red colour of CP **2**. Analogously, d–d transitions at λ > 800 nm are observed (Fig. S20†). This indicates the presence of both, high-spin and low-spin configuration of Fe^{II}.[73–78] Upon increasing temperature, the absorbance at 350–600 nm decreases.

On the contrary, the intensity of the d–d transition band increases, indicating a continuous spin crossover (SCO) from low-spin to high-spin. Since the intensity decrease is more pro-

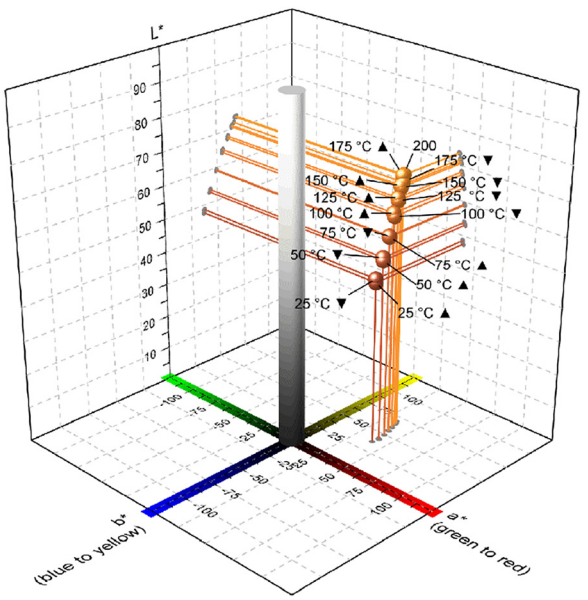

Fig. 10 *L*a*b** scatter diagram with inserted *L*a*b** chromaticity coordinates of $^1_\infty$[Fe(pt)$_2$] (CP **2**) at different measurement temperatures. Recorded points during heating up are marked with ▲. Accordingly, corresponding points recorded with decreasing temperature are marked with ▼. Corresponding *L*a*b** chromaticity values are listed in Table S17.†

nounced for absorbance in the green region, the colour of the compound is shifted from blood red to orange/yellow (Fig. 10, Fig. S21, and Table S17†). Such thermochromic behaviour is known for Fe(II) complexes with octahedral FeN_6 coordination.[73–78]

Investigations on the formation and crystal structures of complexes $[MX_2(Hpt)_2]$

In addition to the homoleptic coordination polymers, several heteroleptic complex compounds were obtained and characterised.

Single crystals of the heteroleptic complexes $[MX_2(Hpt)_2]$ (MX_2 = $MnCl_2$ (**9**), $FeCl_2$ (**10**), $CoCl_2$ (**11**), $CoBr_2$ (**12**)) were obtained by solvothermal reaction of divalent transition metal halides and an excess of Hpt in pyridine without addition of a base, wherefore the ligand remains neutral within the compounds, different from the deprotonated form in **1–8**. Single crystals of $[ZnCl_2(Hpt)_2]$ (**13**) were found within the product of the single crystal preparation of $^1_\infty[Zn(pt)_2]$ (**6**).

The isotypic complexes $[MX_2(Hpt)_2]$ (MX_2 = $MnCl_2$ (**9**), $FeCl_2$ (**10**), $CoCl_2$ (**11**), $CoBr_2$ (**12**), $ZnCl_2$ (**13**)) crystallise in the triclinic crystal system in the space group $P\bar{1}$. The respective metal ions are coordinated *trans* in a distorted octahedral geometry by two halido ligands and two η^2-Hpt molecules binding *via* N1 of the pyridine ring and N4 of the triazole ring.

The complexes are interconnected by N3–H3···Cl1 hydrogen bonds.

A depiction of the crystal structure is exemplarily shown for $[MnCl_2(Hpt)_2]$ (**9**) in Fig. 11. Crystallographic data for **9–13** is given in Tables S5, S7, S9, S11, and S13.† Interatomic distances and angles are listed in Tables S6, S8, S10, S12, and S14.† Mn–N distances for **9** were determined to 223.7(2) pm, and 225.2(2) pm, which are comparable to distances reported for *e.g.* $[Mn_4(H_3bpa)_2(mpt)_4(N_3)_2]\cdot 2H_2O$ (219–238 pm, H_3bpa = *N*,*N*′-bis(picolinamide)azine). This compound contains the Hpt derivative mpt = 3-methyl-5-(2-pyridyl)-1*H*-1,2,4-triazolate and exhibits three crystallographically independent octahedrally coordinated Mn^{2+} ions.[46] Analogously, for the two-dimensional coordination polymer $[Mn(N_3)(pytr)(H_2O)]_n$. (pytr = pt), which contains octahedrally coordinated Mn interconnected by N_3^-, interatomic Mn–N distances to the η^2-pt ligand of 213–223 pm are reported.[79]

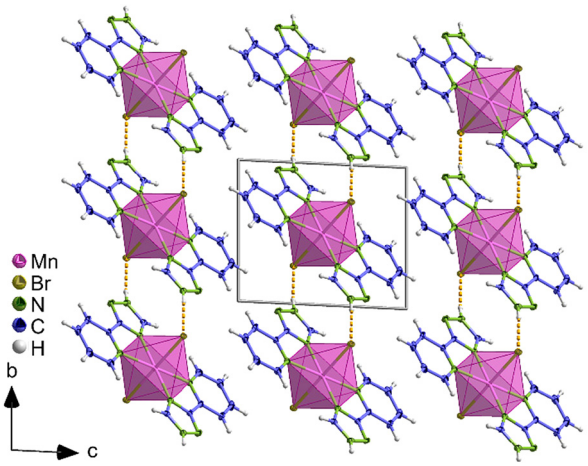

Fig. 11 Depiction of the crystal structure of $[MnCl_2(Hpt)_2]$ (**9**) along the crystallographic *a* axis. The octahedral coordination of Mn^{2+} is highlighted in pink. Displayed thermal ellipsoids correspond to 50% probability level of the atoms. N–H···Cl hydrogen bonds are shown in dashed orange lines. Crystallographic data is summarised in Table S5.† Symmetry operations: I = 1 − *x*, 1 − *y*, 1 − *z*.

In case of $[FeCl_2(Hpt)_2]$ (**10**), the Fe–N distances of 218.48(8) pm and 220.20(8) pm coincide with the 213–223 pm in $[Fe(Hpt)_3](BF_4)_2\cdot H_2O$,[43] which contains Fe^{2+} octahedrally coordinated by three η^2-Hpt ligands.[43] For the complexes $[CoCl_2(Hpt)_2]$ (**11**), and $[CoBr_2(Hpt)_2]$ (**12**), respectively, the distances 213.6(6) pm and 214.6(2) pm for **11**, and 213.4(2) pm and 218.8(2) pm for **12**, are in good agreement to distances in $[Co(Hpt)_2(H_2O)_2](NO_3)_2$ (215 and 216 pm), which contains Co ions coordinated *trans* in an octahedral geometry by two aquo ligands and two η^2-Hpt molecules.[45]

The Zn–N distances in $[ZnCl_2(Hpt)_2]$ (**13**), 214.0(2) pm and 215.7(1) pm, are in the range of Zn–pt distances observed for $[ZnL(pt)]\cdot 0.5MeOH\cdot 1.5H_2O$ (200–225 pm; with L = tris(5-methyl-3-phenylpyrazolyl)borate), which features a fivefold coordinated Zn^{2+}.[44] Alternatively, to the synthesis described above, the complexes **9–13** can be synthesised by choosing acetonitrile instead of pyridine as a non-basic solvent. Due to a lower solubility of the ligand, sublimation of excess Hpt is necessary after the reaction for the products' purification.

Additionally, synthesis utilising water-free chlorides or corresponding hydrates is also feasible (see Experimental section and Fig. 12).

Analogous reactions of $FeBr_2$ and Hpt in either pyridine, or acetonitrile result in phase mixtures containing $^1_\infty[Fe(pt)_2]$ (**2**) and $[FeBr_2(Hpt)_2]$, which is isotypic to $[FeCl_2(Hpt)_2]$ (**10**). Reactions of FeI_2 also result in phase mixtures containing $^1_\infty[Fe(pt)_2]$ (**2**) and $[FeI_2(Hpt)_2]$, which again is isotypic to $[FeCl_2(Hpt)_2]$ (10). Therefore, the existence of $[FeBr_2(Hpt)_2]$, and $[FeI_2(Hpt)_2]$, both being isotypic to **10**, was proven by PXRD (see ESI†).

Accordingly, reactions of $ZnCl_2$ and Hpt in either pyridine, or acetonitrile result in phase mixtures containing $^1_\infty[Zn(pt)_2]$ (**6**). In case of the product synthesised in acetonitrile, $[ZnCl_2(Hpt)_2]$ (**13**) is also contained within the product, as shown by PXRD.

Infrared spectroscopy

The synthesised coordination polymers $^1_\infty[M(pt)_2]$ (M = Mn (**1**), Fe (**2**), Co (**3**), Ni (**4**), Zn (**6**), Cd (**7**)), as well as the complexes $[MX_2(Hpt)_2]$ (MX_2 = $MnCl_2$ (**9**), $FeCl_2$ (**10**), $CoCl_2$ (**11**), $CoBr_2$ (**12**)) were also characterised by infrared spectroscopy. For **1–7**, respective spectra (Fig. S31†) feature bands being characteristic for functional groups of the ligand, as well as the solvents being present within the square-shaped pore channels. The broad band around 3400 nm can be assigned to both, ν(O–H) of intercalated water and ν(N–H) due to established C–H···N hydrogen bonds. For **9**, **10**, **11**, and **12**, bands of the neutral ligand are observable, as well (Fig. S32†). Wavenumbers of observed bands, as well as assignments of those are listed in Tables S22, and S23.†

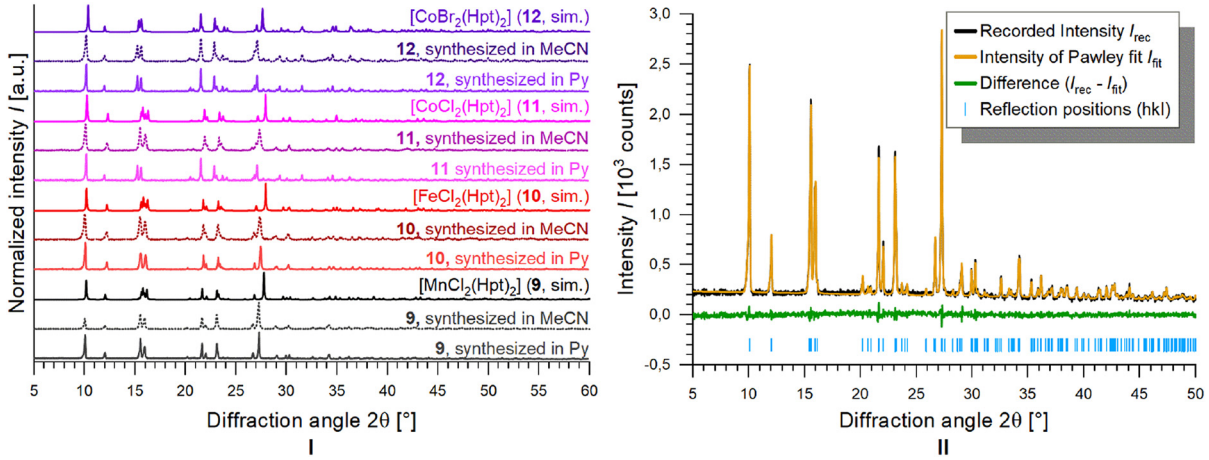

Fig. 12 I: Comparison of recorded and simulated PXRD patterns of the heteroleptic complexes $[MX_2(Hpt)_2]$ (MX_2 = $MnCl_2$ (**9**), $FeCl_2$ (**10**), $CoCl_2$ (**11**), $CoBr_2$ (**12**)), (sim., utilising SCXRD data). The complexes were obtained by synthesis is in the stated solvents (Py = pyridine, solid lines; MeCN = acetonitrile, dotted lines) II: Difference plot of a Pawley refinement exemplarily performed for **9** with an R_{wp} of 6.3% and a goodness of fit of 1.03.

Composition and thermal analyses

Elemental analysis of the synthesised coordination polymers $^1_\infty[M(pt)_2]$ (**1–7**) confirm the assumption of intercalated solvent molecules (pyridine and water). For CPs **1–7**, sum formulas considering amounts of solvents were calculated (Table S24†). Elemental analyses of the complexes $[MnCl_2(Hpt)_2]$ (**9**), $[FeCl_2(Hpt)_2]$ (**10**), $[CoCl_2(Hpt)_2]$ (**11**), and $[CoBr_2(Hpt)_2]$ (**12**) synthesised in pyridine confirm the phase purity already assumed from PXRD results, since calculated and determined elemental percentages are in good agreement (Table S25†). The same applies for complexes **9**, **10**, **11**, and **12** synthesised in acetonitrile (Table S25†).

By simultaneous thermal analysis, $^1_\infty[Mn(pt)_2]$ (**1**), $^1_\infty[Co(pt)_2]$ (**3**), $^1_\infty[Ni(pt)_2]$ (**4**), and $^1_\infty[Zn(pt)_2]$ (**6**) were further investigated. In all cases, the relative mass decreases by 3–7% for temperatures up to approx. 130 °C followed by a plateau. This is considered to be an effect of solvent molecules escaping the solids. Upon further heating, subsequent to the plateau, a significant decrease in relative mass is detected for all investigated CPs, coinciding with a detection of water and carbon dioxide and/or nitrous oxide by mass spectrometry. This indicates an oxidation of the corresponding CP. Thereby, Hpt is combusted, leading to detection of H_2O, and CO_2/N_2O (Fig. S33–S36†). An overview of onsets and relative mass losses determined by STA is given within ESI (Table S26†). The obtained results are in good agreement with the high temperature behaviour of these CPs observed by temperature-dependent PXRD (Fig. 3, and Fig. S6–S18†).

Physisorption experiments on $^1_\infty[M(pt)_2]$ (M = Fe (2), Co (3), Zn (6))

To investigate the inner surface area of the CPs 2, 3, and 6, they were activated at 300 °C and 10^{-3} mbar for seven hours to remove solvent molecules from the pores. The samples were further degassed at 10^{-6} mbar. Subsequently, the inner surface area was determined by recording gas sorption isotherms of N_2 at 77 K (Fig. S37†).

The determined surface areas for BET and Langmuir are listed in Table 2. The determined, high C constants (>150) are considered to be an effect of filling narrow micropores,[80] which is consistent with the square-shaped pore channels observed by SCXRD.

Identification of additional compounds

Besides the coordination compounds described above, a series of additional compounds were identified. Since, in most of the cases, those are considered as intermediates or byproducts, the description of synthesis conditions and single crystal characterizations are discussed in the ESI.† This includes synthesis and SCXRD characterization of the homoleptic complex $[Zr(pt)_4]$ (**14**), the dinuclear complexes $[Fe_2Cl_2(pt)_2(Py)_4]$ (**15**) and $[Fe_2Br_2Cl_2(pt)_2(Py)_4]$ (**16**), the two-dimensional CP $^2_\infty[Cu_2Cl(pt)]$ (**17**), the one-dimensional CPs $^1_\infty[MnCl(bpt)]$ (bpt = 3,5-bis(2-pyridyl)-1,2,4-triazolate, **18**) and $^1_\infty[Co_2Cl_3(pt)(H_2O)_2]\cdot 4CyOH$ (CyOH = cyclohexanol, **19**), an finally the two-dimensional coordination polymer $^2_\infty[Co_2Br_2(pt)_2]$ (**20**).

Experimental

Synthesis procedure

Within this work, solvothermal syntheses were performed according to the following procedure: solid components were mortared and transferred into Duran® glass ampoules. Liquid

Table 2 Multipoint BET surface areas SA_{BET}, C constants for BET calculations, and Langmuir surface areas SA_L of $^1_\infty[M(pt)_2]$ (M = Mn (**1**), Co (**3**), Zn (**6**))

CP	SA_{BET} [$m^2\ g^{-1}$]	C constant	SA_L [$m^2\ g^{-1}$]
$^1_\infty[Fe(pt)_2]$ (**2**)	217	181	286
$^1_\infty[Co(pt)_2]$ (**3**)	181	868	208
$^1_\infty[Zn(pt)_2]$ (**6**)	160	247	210

components and solvents were added, and the resulting mixture was frozen in liquid nitrogen. The ampoules were evacuated, and the mixtures were allowed to thaw again. This freeze–pump–thaw procedure was repeated, followed by freezing the mixture, evacuating the ampoule, and sealing it. The reaction mixtures within the sealed ampoules were homogenised by ultrasonication for three minutes. Afterwards, the ampoules were placed in resistance ovens with corundum tube and heated for several days. For single crystal X-ray diffraction (SCXRD) measurements, the ampoules were opened, and a small amount of the resulting products was isolated. In case of bulk syntheses, the ampoules were opened, the solids were transformed into centrifugation tubes and were washed by repeated centrifugation, decantation, and suspension in fresh solvent. The purified solids were dried for one hour under vacuum (10^{-3} mbar). In case of usage of air-sensitive compounds (e.g. anhydrous metal halides), mortaring and tranferring the mixtures to ampoules were carried out under inert atmosphere.

Materials

2-(1,2,4-1*H*-Triazol-3-yl)pyridine (98%, BLD Pharmatech GmbH), europium(III) nitrate hexahydrate ($Eu(NO_3)_3{\cdot}6H_2O$, 99.9% (REO), abcr GmbH), terbium(III) nitrate hexahydrate ($Tb(NO_3)_3{\cdot}6H_2O$, 99.9% (REO), abcr GmbH), $Mn(OAc)_2{\cdot}4H_2O$ (99%, abcr GmbH), $Fe(OAc)_2$ (anhydrous, 97%, abcr GmbH), $Co(OAc)_2{\cdot}4H_2O$ (98%, abcr GmbH), $Ni(OAc)_2{\cdot}4H_2O$ (98+%, Alfa Aesar), $Cu(OAc)_2{\cdot}H_2O$ (p.a., Riedel-de Haën AG), $Zn(OAc)_2{\cdot}2H_2O$ (p.a., Merck), $Cd(OAc)_2{\cdot}2H_2O$ (98%, abcr GmbH), $MnCl_2$ (99.99%, Alfa Aesar), $FeCl_2$ (anhydrous, 99.5%, Alfa Aesar), $FeBr_2$ (anhydrous, 98%, abcr GmbH), FeI_2 (ultra-dry, 99.99%, abcr GmbH), $CoCl_2$ (99+%, abcr GmbH), $CoBr_2$ (anhydrous, 97%, Alfa Aesar), $CuCl_2$ (anhydrous, 98%, abcr GmbH), $ZnCl_2$ (anhydrous, 98+%, Alfa Aesar), $ZrCl_4$ (anhydrous, 99.5+%, Alfa Aesar), benzylamine (99.5+%, dry, AcroSeal™, Acros Organics), benzene (99.0%, dry, AcroSeal™, Acros Organics), acetonitrile (99.9%, extra dry, AcroSeal™, Acros Organics) and pyridine (99%, VWR Chemicals) were used as purchased without further purification. When dry pyridine is specified, it was dried by stirring over 20 g L^{-1} KOH for several days and distilled under inert atmosphere.

Bulk synthesis of one-dimensional coordination polymers $^1_\infty[M(pt)_2]$ (1–7)

Larger quantities of the coordination polymers $^1_\infty[M(pt)_2]$ (M = Mn (**1**), Fe (**2**), Co (**3**), Cu (**5**), Zn (**6**), Cd (**7**)) were obtained by solvothermally combining 500 μmol (123 mg) $Mn(OAc)_2{\cdot}4H_2O$, (87.0 mg) $Fe(OAc)_2$, (125 mg) $Co(OAc)_2{\cdot}4H_2O$, (99.8) $Cu(OAc)_2{\cdot}H_2O$, (114 mg) $Zn(OAc)_2{\cdot}2H_2O$, or (125 mg) $Cd(OAc)_2{\cdot}2H_2O$ with 1.00 mmol (146 mg) 2-(1,2,4-1*H*-triazol-3-yl) pyridine in 4 mL pyridine following the general synthesis principle mentioned above. In case of $^1_\infty[Ni(pt)_2]$ (**4**), 1.00 mmol (249 mg) $Ni(OAc)_2{\cdot}4H_2O$ and 2.00 mmol (292 mg) 2-(1,2,4-1*H*-triazol-3-yl)pyridine were used. The reaction mixtures were heated to 150 °C in 4 h, followed by heating to 180 °C with 2 °C h^{-1}. This temperature was held constant for 120 h. Subsequently, the reaction mixtures were allowed to cool down to 150 °C with 2 °C h^{-1}, and to ambient temperature within 4 h. Obtained products were purified by centrifugation (12 000 rpm, 10 min), decantation of the liquid phase, addition of 4 mL fresh pyridine and ultrasonication for 10 min. Subsequent to a final centrifugation (12000 rpm, 10 min) and solvent decantation, the products were vacuum-dried at 10^{-3} mbar. The yields were 49% for **1**, 52% for **2**, 77% for **3**, 61% for **4**, 65% for **5**, 42% for **6**, and 58% for **7**, based on the corresponding metal acetate(s) and the sum formulae considering solvent molecules, as listed in Table S24.†

$^1_\infty[Mn(pt)_2]$ (**1**): IR (KBr): $\bar{\nu}$ = 3419 (br), 3030 (multiple, m), 1604 (s), 1513 (m), 1472(s), 1449 (s), 1417 (s), 1384 (w), 1350 (m), 1271 (m), 1250 (m), 1203 (m), 1145 (m), 1112 (s), 1048 (m), 1029 (s), 1007 (m), 876 (m), 805 (m), 755 (m), 676 (m), 636 (m), 483 (m), 407 cm^{-1} (m). Anal. calcd for $^1_\infty[Mn(pt)_2]{\cdot}0.34Py{\cdot}0.21H_2O = C_{15.70}H_{12.12}MnN_{8.34}O_{0.21}$: C 50.19, H 3.25, N 31.07; found: C 50.20, H 2.99, N 30.98.

$^1_\infty[Fe(pt)_2]$ (**2**): $\bar{\nu}$ = 3423 (br), 3030 (multiple, m), 1605 (s), 1516 (m), 1471(s), 1448 (s), 1417 (s), 1384 (w), 1357 (m), 1274 (m), 1252 (m), 1201 (m), 1149 (m), 1115 (s), 1050 (m), 1031 (s), 1009 (m), 874 (m), 803 (m), 757 (m), 676 (m), 636 (m), 490 (m), 409 cm^{-1} (m). Anal. calcd for $^1_\infty[Fe(pt)_2]{\cdot}0.34Py{\cdot}0.21H_2O = C_{15.7}H_{12.12}FeN_{8.34}O_{0.21}$: C 50.04, H 3.24, N 31.00; found: C 50.02, H 2.96, N 30.91.

$^1_\infty[Co(pt)_2]$ (**3**): $\bar{\nu}$ = 3445 (br), 3034 (multiple, m), 1608 (s), 1516 (m), 1473(s), 1449 (s), 1419 (s), 1384 (w), 1360 (m), 1264 (m), 1252 (m), 1204 (m), 1149 (m), 1118 (s), 1050 (m), 1033 (s), 1009 (m), 874 (m), 805 (m), 757 (m), 674 (m), 638 (m), 496 (m), 411 cm^{-1} (m). Anal. calcd for $^1_\infty[Co(pt)_2]{\cdot}0.34Py{\cdot}0.21H_2O = C_{15.7}H_{12.12}CoN_{8.34}O_{0.21}$: C: 49.65, H 3.22, N 30.74; found: C 49.82, H 2.93, N 30.96.

$^1_\infty[Ni(pt)_2]$ (**4**): $\bar{\nu}$ = 3423 (br), 3037 (multiple, w), 1608 (s), 1519 (m), 1473 (s), 1451 (s), 1418 (s), 1391 (w), 1367 (m), 1267 (m), 1254 (m), 1206 (m), 1150 (m), 1126 (s), 1051 (m), 1034 (s), 1012 (m), 871 (m), 803 (m), 757 (m), 676 (m), 639 (m), 502 (m), 415 cm^{-1} (m). Anal. calcd for $^1_\infty[Ni(pt)_2]{\cdot}0.11Py{\cdot}0.63H_2O = C_{14.55}H_{11.81}N_{8.11}NiO_{0.63}$: C 47.38, H 3.23, N 30.78; found: C 47.37, H 3.20, N 30.88.

$^1_\infty[Cu(pt)_2]$ (**5**): $\bar{\nu}$ = 3441 (br), 3031 (multiple, m), 1612 (s), 1598 (s), 1573 (m), 1517 (w), 1471 (s), 1452 (s), 1420 (s), 1369 (m), 1352 (m), 1286 (m), 1268 (m), 1252 (m), 1208 (w), 1137 (m), 1121 (s), 1095 (m), 1042 (m), 1022 (m), 998 (m), 870 (m), 801 (m), 752 (m), 676 (m), 723(s), 702 (m), 677 (m), 665 (m), 642 (m), 628 (m) 490 (w), 408 cm^{-1} (w). Anal. calcd for $^1_\infty[Cu(pt)_2]{\cdot}0.05Py{\cdot}0.63H_2O = C_{14.25}H_{11.51}N_{8.05}CuO_{0.63}$: C 46.38, 3.14, N 30.55; found: C 46.07, H 2.78, N 29.64.

$^1_\infty[Zn(pt)_2]$ (**6**): $\bar{\nu}$ = 3421 (br), 3035 (multiple, m), 1605 (s), 1517 (m), 1476 (s), 1451 (s), 1438 (s), 1421 (s), 1391 (w), 1363 (m), 1265 (m), 1252 (m), 1208 (m), 1149 (m), 1125 (s), 1050 (m), 1035 (s), 1007 (m), 876 (m), 806 (m), 755 (m), 674 (m), 635 (m), 493 (m), 408 cm^{-1} (m). Anal. calcd for $^1_\infty[Zn(pt)_2]{\cdot}0.39Py{\cdot}0.63H_2O = C_{16.05}H_{13.31}N_{8.41}O_{0.63}Zn$: C 48.15, H 3.34, N 29.55; found: C 48.31, H 2.96, N 29.53.

$^1_\infty[Cd(pt)_2]$ (**7**): $\bar{\nu}$ = 3421 (br), 3035 (multiple, m), 1605 (s), 1517 (m), 1476 (s), 1451 (s), 1438 (s), 1421 (s), 1391 (w), 1363

(m), 1265 (m), 1252 (m), 1208 (m), 1149 (m), 1125 (s), 1050 (m), 1035 (s), 1007 (m), 876 (m), 806 (m), 755 (m), 674 (m), 635 (m), 493 (m), 408 cm^{-1} (m). Anal. calcd for $^{1}_{\infty}$[Cd(pt)$_2$]·0.24Py·0.63H_2O = $C_{15.20}H_{12.46}N_{8.24}CdO_{0.63}$: C 42.15, H 2.90, N 26.66; found: C 41.97, H 2.53, N 26.26.

Synthesis of single crystals of $^{1}_{\infty}$[Zn(pt)$_2$] (6)

Single crystals suitable for single crystal X-ray diffraction (SCXRD) of CP 6 were obtained by reaction of 55 μmol (7.5 mg) of water-free $ZnCl_2$, 0.15 mmol (22 mg) of 2-(1,2,4-1*H*-triazol-3-yl)pyridine (Hpt), and 2 droplets of benzylamine according to the procedure described above. A mixture of 0.9 mL water-free toluene and 0.1 mL water-free pyridine was used as solvent. The reaction mixture was heated to 180 °C with 2 °C h^{-1} and held constant at this temperature for 480 h. Subsequently the mixture was allowed to cool down to ambient temperature with 2 °C h^{-1}.

Synthesis of single crystals of $^{1}_{\infty}$[Cu(pt)$_2$]·0.5Py (8)

Single crystals suitable for SCXRD of CP 8 were obtained by reaction of 0.46 mmol (91 mg) Cu(OAc)$_2$·H_2O and 1.00 mmol (146 mg) 2-(1,2,4-1*H*-triazol-3-yl)pyridine (Hpt) in 4 mL pyridine following the general synthesis principle mentioned above. The reaction mixture was heated to 150 °C in 4 h, followed by heating to 180 °C with 2 °C h^{-1}. This temperature was held constant for 120 h. Subsequently, the reaction mixture was allowed to cool down to 150 °C with 2 °C h^{-1}, and to ambient temperature within 4 h. It is noteworthy that this synthesis is analogous to the bulk synthesis of $^{1}_{\infty}$[M(pt)$_2$] (**1–7**) but *without* vacuum-drying of the obtained product. Consequently, CP **8** is only existent when still damp. Upon drying, the obtained product converts to **5**.

Impregnation of $^{1}_{\infty}$[Zn(pt)$_2$] (6) with Eu and Tb

$^{1}_{\infty}$[Zn(pt)$_2$] (**6**) was activated at 300 °C for seven hours at 10^{-3} mbar. Subsequently, three samples of 15 mg (42 μmol) of the activated polymer were each dispersed in a solution of 18 mg (40 μmol) $EuNO_3$·6H_2O and 18 mg (40 μmol) Tb(NO$_3$)$_3$·6H_2O in 4 mL DMF, MeCN or MeOH. The resulting suspensions were homogenised by ultrasonication for ten minutes and were magnetically stirred for eight days. Afterwards, the solids were separated from the liquid phase by centrifugation (10 000 rpm, 10 min) and decantation of the solution. The obtained solids were dried in vacuum (10^{-3} mbar) for one hour.

Bulk syntheses of complexes [MX$_2$(Hpt)$_2$] (MX$_2$ = MnCl$_2$ (9) and FeCl$_2$ (10))

1.00 mmol (126 mg) $MnCl_2$ or (127 mg) $FeCl_2$ were reacted with 2.40 mmol (351 mg) 2-(1,2,4-1*H*-triazol-3-yl)pyridine (Hpt) in 0.5 mL pyridine following the general synthesis principle mentioned above under inert atmosphere. The reaction mixture was heated to 150 °C within four hours, followed by heating up to 200 °C with 2 °C h^{-1}. This temperature was held constant for 120 h. Subsequently, the mixture was allowed to cool down to 150 °C with 2 °C h^{-1} and then to room temperature within four hours. The liquid phase was removed manually under inert atmosphere, and the obtained solid was dried in vacuum (10^{-3} mbar). The yield was 73% for **9** and 77% for **10**, based on the corresponding metal halide.

[$MnCl_2$(Hpt)] (**9**): $\bar{\nu}$ = 3450 (br), 3079 (s), 2994 (s), 2891 (s), 1816 (m), 1657 (m), 1603 (s), 1569 (m), 1537 (m), 1503 (s), 1477 (s), 1448 (s), 1422 (s), 1340 (s), 1289 (s), 1272 (s), 1188 (m), 1149 (m), 1133 (m), 1098 (m), 1085 (m), 1051 (s), 1016 (m), 993 (s), 974 (m), 912 (m), 846 (s), 797 (s), 749 (s), 724 (s), 714 (s), 639 (s), 479 (m), 412 cm^{-1} (m). Anal. calcd for [$MnCl_2$(Hpt)$_2$] = $C_{14}H_{12}Cl_2MnN_8$: C 40.32, H 2.30, N 26.80; found: C 40.06, H 2.70, N 26.19.

[$FeCl_2$(Hpt)] (**10**): $\bar{\nu}$ = 3442 (br), 3085 (s), 3006 (s), 2901 (s), 1809 (w), 1639 (m), 1605 (s), 1569 (w), 1540 (m), 1503 (s), 1482 (m), 1448 (m), 1425 (s), 1341 (s), 1288 (s), 1271 (s), 1190 (m), 1150 (m), 1136 (m), 1098 (w), 1085 (m), 1051 (m), 1016 (m), 994 (s), 976 (m), 908 (m), 836 (s), 797 (m), 751 (s), 724 (s), 715 (m), 639 (s), 486 (m), 415 cm^{-1} (m). Anal. calcd for [$FeCl_2$(Hpt)$_2$] = $C_{14}H_{12}Cl_2FeN_8$: C 40.13, 2.89, N 26.74; found: C 40.87, H 2.80, N 26.43.

Synthesis of single crystals of [MnCl$_2$(Hpt)$_2$] (9) and [FeCl$_2$(Hpt)$_2$] (10)

Crystals suitable for SCXRD of the isotypic complexes 9 and 10 were obtained by solvothermal reaction of 0.20 mmol (25 mg) $MnCl_2$ or $FeCl_2$ and 0.48 mmol (70 mg) 2-(1,2,4-1*H*-triazol-3-yl) pyridine (Hpt) in 0.3 mL pyridine following the procedure described above. The reaction mixture was heated to 150 °C within 4 h, followed by heating to 200 °C with 2 °C h^{-1}. This temperature was held for 120 h. Subsequently the mixture was allowed to cool down to 150 °C with 2 °C h^{-1}, and to ambient temperature within 4 h.

Bulk syntheses of [MX$_2$(Hpt)$_2$] (MX$_2$ = CoCl$_2$ (11) and CoBr$_2$ (12))

0.40 mmol (52 mg) $CoCl_2$, or (88 mg) $CoBr_2$ were reacted with 1.00 mmol (146 mg) 2-(1,2,4-1*H*-triazol-3-yl)pyridine (Hpt) in 1 mL acetonitrile following the general synthesis principle mentioned above under inert atmosphere. The reaction mixture was heated up to 115 °C within four hours. This temperature was held constant for 144 h followed by cooling down to room temperature within four hours. The liquid phase was manually removed under inert atmosphere and the obtained solid was vacuum-dried at 10^{-3} mbar. Excess ligand was separated from the product by sublimation at 150 °C for five days. The yield was 74% for **11** and 87% for **12**, based on the corresponding metal halide.

[$CoCl_2$(Hpt)] (**11**): $\bar{\nu}$ = 3085 (s), 2997 (s), 2892 (s), 1807 (w), 1657 (m), 1608 (s), 1569 (w), 1542 (w), 1504 (s), 1479 (m), 1449 (m), 1426 (m), 1344 (m), 1289 (m), 1271 (m), 1193 (w), 1152 (w), 1139 (m), 1099 (w), 1088 (w), 1051 (m), 1018 (m), 996 (m), 976 (m), 907 (w), 844 (s), 797 (m), 752 (m), 724 (s), 717 (m), 639 (m), 490 (w), 419 cm^{-1} (w). Anal. calcd for $C_{14}H_{12}Cl_2CoN_8$: C 39.83, H 2.87, N 26.54; found: C 40.29, H 2.57, N 26.47.

[$CoBr_2$(Hpt)] (**12**): 3432 (br), 3085 (s), 3011 (s), 2898 (s), 1788 (w), 1635 (w), 1606 (s), 1569 (m), 1542 (w), 1501 (s), 1477 (s), 1448 (s), 1423 (s), 1341 (m), 1285 (s), 1265 (s), 1212 (m), 1190

(m), 1149 (m), 1137 (m), 1118 (m), 1098 (m), 1086 (m), 1067 (w), 1051 (m), 1031 (w), 1017 (m), 1006 (m), 996 (m), 974 (m), 923 (w), 899 (w), 894 (w), 874 (w), 817 (s), 797 (m), 752 (s), 724 (s), 717 (m), 676 (w), 635 (m), 490 (w), 419 cm^{-1} (w) (Recorded for a product synthesised in pyridine). Anal. calcd for $C_{14}H_{12}Br_2CoN_8$: C 32.90, H 2.37, N 21.93; found: C 32.40, H 2.23, N 20.96.

Synthesis of single crystals of $[CoCl_2(Hpt)_2]$ (11) and $[CoBr_2(Hpt)_2]$ (12)

Crystals suitable for SCXRD of the isotypic complexes 13 and 14 were obtained by solvothermal reaction of 0.50 mmol (65 mg) $CoCl_2$ or (0.11 g) $CoBr_2$ and 1.20 mmol (176 mg) 2-(1,2,4-1*H*-triazol-3-yl)pyridine (Hpt) in 0.3 mL pyridine following the procedure described above. The reaction mixture was thermally treated in analogy to the synthesis of 9 and 10.

Synthesis of single crystals of $[ZnCl_2(Hpt)_2]$ (13)

Single crystals of **13** were found within the solid product, in which crystals of $^1_\infty[Zn(pt)_2]$ (**6**) were found, as well (see above).

Conclusions

Within this work, coordination compounds based on divalent 3d-transition metal ions and the ligand 2-(1,2,4-1*H*-triazol-3-yl) pyridine (Hpt) were synthesised. Altogether, 12 fully characterised compounds and the structures of eight more that were obtained as side products are reported. The deprotonated ligand is able to interconnect transition metal ions (here Mn^{2+}, Fe^{2+}; Co^{2+}, Ni^{2+}, Cu^{2+}, Zn^{2+}, Cd^{2+}) to form homoleptic one-dimensional coordination polymers (CPs) with a generalised sum formula of $^1_\infty[M(pt)_2]$, which are stable to temperatures up to 300–400 °C, depending on the metal ion. Considering C–H···N interactions between the polymeric strands, the CPs can be described supermolecular three-dimensional structures exhibiting square-shaped channel pores, in which solvent molecules are intercalated from the syntheses, as shown by temperature-dependent PXRD, STA and elemental analyses.

Besides colourful products containing Fe, Co, Ni, and Cu, the polymers containing Mn and Zn are colourless solids. Especially for $^1_\infty[Zn(pt)_2]$, this appearance – in combination with UV absorption and ligand-based blue light emission of the CP – allows creation of a white light-emitter according to the RGB concept by activation of the CP and subsequent impregnation with Eu^{3+} and Tb^{3+}. The colour of the emitted light can be tuned from neon blue to practically perfect white light by choosing an appropriate excitation wavelength. Furthermore, the coordination polymer $^1_\infty[Fe(pt)_2]$ shows thermochromic behaviour based on continuous spin crossover. In addition to the homoleptic coordination polymers, several mononuclear complexes $[MX_2(Hpt)_2]$ and numerous crystalline by-products were found and their structures determined. They illuminate a product rich chemistry of the ligand Hpt with transition metal ions.

Data availability

Single crystal structures determined within the scope of this work were uploaded to the CCDC database.CCDC 2347927 (**6**), 2347920 (**8**), 2347949 (**9**), 2347948 (**10**), 2347938 (**11**), 2347937 (**12**), 2347952 (**13**), 2347953 (**14**), 2347947 (**15**), 2347946 (**16**), 2347951 (**17**), 2347925 (**18**), 2347917 (**19**), and 2347950 (**20**).

In addition, the ESI† (62 pages) contains detailed description of analytical methods used, tables with crystallographic data, selected interatomic distances and angles, UV-Vis spectra, photoluminescence spectra, IR spectra, powder X-ray diffraction plots, simultaneous thermal analysis graphs, sorption isotherms, and additional experiments and single crystal structures description. Besides references cited in the main paper, the authors have cited additional references within the ESI.†[41,43,46,56–60,62,69,70,81]

Conflicts of interest

There are no conflicts to declare.

Acknowledgements

The authors thank Lisa-Marie Wagner for performing single crystal X-ray diffraction experiments. Furthermore, we gratefully acknowledge *Chemisches Labor Dr. Graser KG* for the opportunity of performing ICP-MS measurements.

References

1 (*a*) J. Malinowski, D. Zych, D. Jacewicz, B. Gawdzik and J. Drzeżdżon, *Int. J. Mol. Sci.*, 2020, **21**, 5443; (*b*) R. Kumar, A. Thakur, Sachin, D. Chandra, A. Kumar Dhiman, P. Kumar Verma and U. Sharma, *Coord. Chem. Rev.*, 2024, **499**, 215453; (*c*) S. Tai, E. J. Dover, S. V. Marchi and J. D. Carrick, *J. Org. Chem.*, 2015, **80**, 6275–6282; (*d*) J. Halpern, *Adv. Chem.*, 1974, **70**, 1–24.
2 R. H. Elattar, S. F. El-Malla, A. H. Kamal and F. R. Mansour, *Coord. Chem. Rev.*, 2024, **501**, 215568.
3 M. Pellei, F. Del Bello, M. Porchia and C. Santini, *Coord. Chem. Rev.*, 2021, **445**, 214088.
4 M. S. A. Mansour, A. T. Abdelkarim, A. A. El-Sherif and W. H. Mahmoud, *BMC Chem.*, 2024, **18**, 150.
5 M. Albqmi, N. A. Elkanzi, A. M. Ali and A. Abdou, *J. Mol. Struct.*, 2025, **1319**, 139494.
6 Y. Senpradit, S. Wacharasindhu and M. Sukwattanasinitt, *Spectrochim. Acta, Part A*, 2025, **326**, 125128.
7 I. Bala, K. Singh, Kiran, R. Kataria and J. Sindhu, *Inorg. Chim. Acta*, 2025, **574**, 122411.
8 Y. Jiao, Y. Li, H. Tang, S. Xian, Y. He, L. Wang and J. Zhang, *J. Photochem. Photobiol., A*, 2025, **458**, 115940.
9 X. Cao, N. Feng, Q. Huang and Y. Liu, *ACS Appl. Bio Mater.*, 2024, **7**, 7965–7986.

10 S. Dilshad, M. Muslim, A. Ahmed, A. Ali, S. Firdaus, M. J. Alam, S. Ahmad, M. Ahmad and A. Ahmad, *J. Mol. Struct.*, 2024, **1301**, 137350.
11 M. N. Khrizanforov, A. A. Zagidullin, R. P. Shekurov, F. F. Akhmatkhanova, I. A. Bezkishko, V. V. Ermolaev and V. A. Miluykov, *Comments Inorg. Chem.*, 2024, **44**, 98–142.
12 Y. Xiong, Q. Feng, L. Lu, X. Qiu, S. Knoedler, A. C. Panayi, D. Jiang, Y. Rinkevich, Z. Lin, B. Mi, G. Liu and Y. Zhao, *Adv. Mater.*, 2024, **36**, e2302587.
13 (*a*) S. J. Lee and S. G. Telfer, *Angew. Chem., Int. Ed.*, 2023, **62**, e202306341; (*b*) C. Janiak and J. K. Vieth, *New J. Chem.*, 2010, **34**, 2366; (*c*) D. J. Tranchemontagne, J. L. Mendoza-Cortés, M. O'Keeffe and O. M. Yaghi, *Chem. Soc. Rev.*, 2009, **38**, 1257–1283.
14 H. Liang, K. Otsubo, Y. Wakabayashi, H. Sagayama, S. Kawaguchi and H. Kitagawa, *Angew. Chem., Int. Ed.*, 2024, e202400162.
15 M. Zhang, R. Tan, M. Wang, Z. Zhang, C. J. Low and Y. Lai, *Battery Energy*, 2024, **3**, 20230050.
16 H. Zhou, H. Wang, C. Yue, L. He, H. Li, H. Zhang, S. Yang and T. Ma, *Appl. Catal., B*, 2024, **344**, 123605.
17 (*a*) Z. Ma, X. Song, Z. Li, Y. Ren, J. Wang and Y. Liang, *Dalton Trans.*, 2024, **53**, 3797–3807; (*b*) M. Kacem and M. Dib, *Inorg. Chem. Commun.*, 2023, **158**, 111561; (*c*) Z. Liu, D. Sun, C. Wang, B. You, B. Li, J. Han, S. Jiang, C. Zhang and S. He, *Coord. Chem. Rev.*, 2024, **502**, 215612.
18 P. Hajivand, J. C. Jansen, E. Pardo, D. Armentano, T. F. Mastropietro and A. Azadmehr, *Coord. Chem. Rev.*, 2024, **501**, 215558.
19 S. Huang, Y. Ye, C. Jiang, R. Wang, W. Hu, S. Raza, J. Ouyang, Y. Pan and J. Liu, *React. Funct. Polym.*, 2023, **193**, 105743.
20 W. Li, X. Liu, X. Yu, B. Zhang, C. Ji, Z. Shi, L. Zhang and Y. Liu, *Inorg. Chem.*, 2023, **62**, 18248–18256.
21 (*a*) W. Liu, H. Cui, J. Zhou, X. Chen, H. Yang and J. Wang, *J. Mol. Struct.*, 2024, **1302**, 137468; (*b*) Y. Qiao, C. Sun, J. Jian, T. Zhou, X. Xue, J. Shi, L. Zhao and G. Liao, *Inorg. Chem.*, 2024, **63**, 2060–2071; (*c*) J.-X. Wang, T.-T. Wu, M.-Q. Tuo, H.-B. Pan, J. Ge, P.-P. Huang, J.-H. Gao, M. Jiang and J.-F. Lu, *Polyhedron*, 2024, **252**, 116884; (*d*) Y.-F. Ma, X.-L. Liu, X.-Y. Lu, M.-L. Zhang, Y.-X. Ren and X.-G. Yang, *Spectrochim. Acta, Part A*, 2024, **309**, 123803.
22 A. J. Amoroso and S. J. A. Pope, *Chem. Soc. Rev.*, 2015, **44**, 4723–4742.
23 (*a*) Z. Gao, B. Xu, T. Zhang, Z. Liu, W. Zhang, X. Sun, Y. Liu, X. Wang, Z. Wang, Y. Yan, F. Hu, X. Meng and Y. S. Zhao, *Angew. Chem., Int. Ed.*, 2020, **59**, 19060–19064; (*b*) C. Sun, R. Xi and H. Fei, *Acc. Chem. Res.*, 2023, **56**, 452–461.
24 (*a*) C. Chiatti, I. Kousis, C. Fabiani and A. L. Pisello, *Renewable Energy*, 2022, **196**, 28–39; (*b*) X. Zhang, D. Liu, J. Yu, X. Li, H. Zheng, Y. Zhou, C. Huang, Y. Zhu, C. Jiao and Z. Sun, *Dalton Trans.*, 2023, **52**, 8558–8566.
25 M. T. Seuffert, S. Wintzheimer, M. Oppmann, T. Granath, J. Prieschl, A. Alrefai, H.-J. Holdt, K. Müller-Buschbaum and K. Mandel, *J. Mater. Chem. C*, 2020, **8**, 16010–16017.
26 P. Falcaro and S. Furukawa, *Angew. Chem., Int. Ed.*, 2012, **51**, 8431–8433.
27 (*a*) P. R. Matthes, C. J. Höller, M. Mai, J. Heck, S. J. Sedlmaier, S. Schmiechen, C. Feldmann, W. Schnick and K. Müller-Buschbaum, *J. Mater. Chem.*, 2012, **22**, 10179; (*b*) Y. Shu, Q. Ye, T. Dai, Q. Xu and X. Hu, *ACS Sens.*, 2021, **6**, 641–658; (*c*) X. Chen and Z. Jiang, *Inorg. Chim. Acta*, 2024, **561**, 121852.
28 S. S. Mondal, K. Behrens, P. R. Matthes, F. Schönfeld, J. Nitsch, A. Steffen, P.-A. Primus, M. U. Kumke, K. Müller-Buschbaum and H.-J. Holdt, *J. Mater. Chem. C*, 2015, **3**, 4623–4631.
29 Y.-B. Hao, Z.-S. Shao, C. Cheng, X.-Y. Xie, J. Zhang, W.-J. Song and H.-S. Wang, *ACS Appl. Mater. Interfaces*, 2019, **11**, 31755–31762.
30 H. P. Toledo-Jaldin, C. Pinzón-Vanegas, A. Blanco-Flores, J. Zamora-Moreno, L. D. Rosales-Vázquez, A. R. Vilchis-Nestor, I. A. Reyes-Domínguez, M. Á. Romero-Solano and A. Dorazco-González, *Environ. Pollut.*, 2024, **343**, 123195.
31 X. Zuo, P. Liu, Q. Sun, J. Huang, Y. Zhang, X. Zhu, R. Chen and X. Meng, *New J. Chem.*, 2024, **48**, 1642–1649.
32 (*a*) S. Yang, Z. Zhou, Z. Zhao, J. Liu, Y. Sun, Y. Zhang, E. Gao, M. Zhu and S. Wu, *Microchem. J.*, 2024, **196**, 109660; (*b*) A. E. Psalti, D. Andriotou, S. A. Diamantis, A. Chatz-Giachia, A. Pournara, M. J. Manos, A. Hatzidimitriou and T. Lazarides, *Inorg. Chem.*, 2022, **61**, 11959–11972; (*c*) Q. Tang, S. Liu, Y. Liu, D. He, J. Miao, X. Wang, Y. Ji and Z. Zheng, *Inorg. Chem.*, 2014, **53**, 289–293; (*d*) J. Xue, Y. Wang, G. Yang and Y. Wang, *J. Rare Earths*, 2024, **42**, 446–454.
33 X.-Y. Xu and B. Yan, *Dalton Trans.*, 2015, **44**, 1178–1185.
34 E. F. Schubert and J. K. Kim, *Science*, 2005, **308**, 1274–1278.
35 W. Cao, Y. Tang, Y. Cui and G. Qian, *Small Struct.*, 2020, **1**, 2000019.
36 N. Alam, S. Mondal, S. S. Hossain, S. Sahoo and D. Sarma, *ACS Appl. Eng. Mater.*, 2023, **1**, 1201–1212.
37 J. Othong, J. Boonmak, V. Promarak, F. Kielar and S. Youngme, *ACS Appl. Mater. Interfaces*, 2019, **11**, 44421–44429.
38 (*a*) V. Raman, M. Y. Borzehandani, M. A. M. Latif, M. I. M. Tahir, M. B. Abdul Rahman and Y. Sulaiman, *Polyhedron*, 2024, **253**, 116890; (*b*) F. A. Brede, J. Heine, G. Sextl and K. Müller-Buschbaum, *Chem. – Eur. J.*, 2016, **22**, 2708–2718; (*c*) M. Smida, J. Lhoste, V. Pimenta, A. Hémon-Ribaud, L. Jouffret, M. Leblanc, M. Dammak, J.-M. Grenèche and V. Maisonneuve, *Dalton Trans.*, 2013, **42**, 15748–15755; (*d*) Y.-G. Huang, B. Mu, P. M. Schoenecker, C. G. Carson, J. R. Karra, Y. Cai and K. S. Walton, *Angew. Chem., Int. Ed.*, 2011, **50**, 436–440; (*e*) G. Wei, Y.-F. Shen, Y.-R. Li and X.-C. Huang, *Inorg. Chem.*, 2010, **49**, 9191–9199; (*f*) W. Ouellette, B. S. Hudson and J. Zubieta, *Inorg. Chem.*, 2007, **46**, 4887–4904; (*g*) W. Ouellette, J. R. Galan-Mascarós, K. R. Dunbar and J. Zubieta, *Inorg. Chem.*, 2006, **45**, 1909–1911; (*h*) J. Kröber, I. Bkouche-Waksman, C. Pascard, M. Thomann and O. Kahn, *Inorg. Chim. Acta*, 1995, **230**, 159–163.

39 (*a*) J. Liu, L. Y. Yang and F. Luo, *J. Solid State Chem.*, 2021, **301**, 122369; (*b*) J.-Y. Zou, L. Li, S.-Y. You, H.-M. Cui, Y.-W. Liu, K.-H. Chen, Y.-H. Chen, J.-Z. Cui and S.-W. Zhang, *Dyes Pigm.*, 2018, **159**, 429–438.
40 C.-H. Li, Y.-L. Li, W. Li and Y.-F. Kuang, *Chin. J. Struct. Chem.*, 2021, **40**, 363.
41 C.-H. Li, W. Li, Y.-L. Li and Y.-Q. Yang, *Chin. J. Struct. Chem.*, 2012, 1089.
42 (*a*) J.-J. Zhang, N.-F. Yang, C.-H. Zhang and B.-H. Li, *Chin. J. Inorg. Chem.*, 2010, **26**, 533–536; (*b*) S. Sarkar, T. Mukherjee, S. Sen, E. Zangrando and P. Chattopadhyay, *J. Mol. Struct.*, 2010, **980**, 117–123.
43 A. F. Stassen, M. de Vos, P. J. van Koningsbruggen, F. Renz, J. Ensling, H. Kooijman, A. L. Spek, J. G. Haasnoot, P. Gütlich and J. Reedijk, *Eur. J. Inorg. Chem.*, 2000, **2000**, 2231–2237.
44 B. L. Dick and S. M. Cohen, *Inorg. Chem.*, 2018, **57**, 9538–9543.
45 C.-C. Du, J.-Z. Fan, J.-P. Li and D.-Z. Wang, *Chin. J. Inorg. Chem.*, 2017, **33**, 1685.
46 L. Cheng, W.-X. Zhang, B.-H. Ye, J.-B. Lin and X.-M. Chen, *Inorg. Chem.*, 2007, **46**, 1135–1143.
47 J. Bergmann, K. Stein, M. Kobalz, M. Handke, M. Lange, J. Möllmer, F. Heinke, O. Oeckler, R. Gläser, R. Staudt and H. Krautscheid, *Microporous Mesoporous Mater.*, 2015, **216**, 56–63.
48 (*a*) Q.-L. Liu, L.-J. Yang, Y.-H. Luo, W. Wang, Y. Ling and B.-W. Sun, *Synth. React. Inorg., Met.-Org., Nano-Met. Chem.*, 2016, **46**, 1725–1734; (*b*) X. Bao, J.-L. Liu, J.-D. Leng, Z. Lin, M.-L. Tong, M. Nihei and H. Oshio, *Chem. – Eur. J.*, 2010, **16**, 7973–7978; (*c*) G.-B. Jiang, X.-N. Zeng, Y.-S. Fang, M.-H. Zeng and S. W. Ng, *Acta Crystallogr., Sect. E: Struct. Rep. Online*, 2007, **63**, m2319.
49 M.-Z. Li, J.-H. Guo and J. Chen, *Z. Anorg. Allg. Chem.*, 2015, **641**, 2581–2586.
50 J.-J. Yan, C.-H. Li, W. Li, Z.-T. Yang, L. Li and H.-B. Liu, *Jiegou Huaxue*, 2019, **38**, 1823.
51 C. Li, H. Gao, L. Li, W. Wei and Y. Tan, *Inorg. Chem. Commun.*, 2020, **111**, 107613.
52 A. V. Kuttatheyil, M. Handke, J. Bergmann, D. Lässig, J. Lincke, J. Haase, M. Bertmer and H. Krautscheid, *Chemistry*, 2015, **21**, 1118–1124.
53 J.-L. Chen, X.-F. Cao, J.-Y. Wang, L.-H. He, Z.-Y. Liu, H.-R. Wen and Z.-N. Chen, *Inorg. Chem.*, 2013, **52**, 9727–9740.
54 A. L. Webber, J. R. Yates, M. Zilka, S. Sturniolo, A.-C. Uldry, E. K. Corlett, C. J. Pickard, M. Pérez-Torralba, M. Angeles Garcia, D. Santa Maria, R. M. Claramunt and S. P. Brown, *J. Phys. Chem. A*, 2020, **124**, 560–572.
55 (*a*) W. Guo, J. Liu, P. G. Weidler, J. Liu, T. Neumann, D. Danilov, W. Wenzel, C. Feldmann and C. Wöll, *Phys. Chem. Chem. Phys.*, 2014, **16**, 17918–17923; (*b*) S. Lee, H.-B. Bürgi, S. A. Alshmimri and O. M. Yaghi, *J. Am. Chem. Soc.*, 2018, **140**, 8958–8964; (*c*) K. Schlichte, T. Kratzke and S. Kaskel, *Microporous Mesoporous Mater.*, 2004, **73**, 81–88; (*d*) A. A. Yakovenko, Z. Wei, M. Wriedt, J.-R. Li, G. J. Halder and H.-C. Zhou, *Cryst. Growth Des.*, 2014, **14**, 5397–5407.
56 H.-K. Mao, T. Takahashi, W. A. Bassett, G. L. Kinsland and L. Merrill, *J. Geophys. Res.*, 1974, **79**, 1165–1170.
57 M. E. Fleet, *Acta Crystallogr., Sect. B: Struct. Crystallogr. Cryst. Chem.*, 1981, **37**, 917–920.
58 L. Pauling and S. B. Hendricks, *J. Am. Chem. Soc.*, 1925, **47**, 781–790.
59 S. Nagakura, *J. Phys. Soc. Jpn.*, 1958, **13**, 1005–1014.
60 P. Scherrer, *Z. Kristallogr. – Cryst. Mater.*, 1922, **57**, 186–189.
61 M. Becker and M. Jansen, *Acta Crystallogr., Sect. C: Cryst. Struct. Commun.*, 2001, **C57**, 347–348.
62 G. Baldinozzi, B. Malinowska, M. Rakib and G. Durand, *J. Mater. Chem.*, 2002, **12**, 268–272.
63 S. A. Sapchenko, D. G. Samsonenko and V. P. Fedin, *Polyhedron*, 2013, **55**, 179–183.
64 Y. Meng, N. Zhang, J. Li, Y. Xu, Q. Yang, Y. Yuan, X. Zhang, J. Wu and L. Zhao, *Spectrochim. Acta, Part A*, 2022, **266**, 120419.
65 E. San Sebastian, A. Rodríguez-Diéguez, J. M. Seco and J. Cepeda, *Eur. J. Inorg. Chem.*, 2018, **2018**, 2155–2174.
66 R. C. Leif, L. M. Vallarino, M. C. Becker and S. Yang, *Cytometry, Part A*, 2006, **69**, 767–778.
67 J.-C. G. Bünzli and C. Piguet, *Chem. Soc. Rev.*, 2005, **34**, 1048–1077.
68 A. de Bettencourt-Dias, *Luminescence of lanthanide ions in coordination compounds and nanomaterials*, Wiley, Chichester, England, 2014, pp. 40–44.
69 A. Sillen and Y. Engelborghs, *Photochem. Photobiol.*, 1998, **67**, 475–486.
70 S. V. Eliseeva and J.-C. G. Bünzli, *Chem. Soc. Rev.*, 2010, **39**, 189–227.
71 M. Pamei and A. Puzari, *Nano-Struct. Nano-Objects*, 2019, **19**, 100364.
72 (*a*) *Lanthanide probes in life, chemical and earth sciences: Theory and practice*, ed. J.-C. G. Bünzli and G. R. Choppin, Elsevier, Amsterdam, 1989; (*b*) J. Maillard, K. Klehs, C. Rumble, E. Vauthey, M. Heilemann and A. Fürstenberg, *Chem. Sci.*, 2020, **12**, 1352–1362.
73 Y. Bayeh, P. Osuský, N. J. Yutronkie, R. Gyepes, A. Sergawie, P. Hrobárik, R. Clérac and M. Thomas, *Polyhedron*, 2022, **227**, 116136.
74 A. E. Thorarinsdottir, A. I. Gaudette and T. D. Harris, *Chem. Sci.*, 2017, **8**, 2448–2456.
75 J. England, G. J. P. Britovsek, N. Rabadia and A. J. P. White, *Inorg. Chem.*, 2007, **46**, 3752–3767.
76 V. Balland, F. Banse, E. Anxolabéhère-Mallart, M. Nierlich and J.-J. Girerd, *Eur. J. Inorg. Chem.*, 2003, **2003**, 2529–2535.
77 *Anorganische Chemie. Prinzipien von Struktur und Reaktivität*, ed. J. Huheey, R. Keiter and E. Keiter, De Gruyter, Inc., Berlin, 5th edn, 2014.
78 *Photochemistry and Photophysics of Coordination Compounds I*, ed. V. Balzani and S. Campagna, Springer Berlin Heidelberg, Berlin, Heidelberg, 2007, vol. 280.
79 X.-L. Xu, P.-F. Yao, Da.-Ye Zhu, H.-Ye Li, H.-Fu Liu and Fu.-P. Huang, *Chin. J. Struct. Chem.*, 2017, **36**, 958.

80 M. Thommes, K. Kaneko, A. V. Neimark, J. P. Olivier, F. Rodriguez-Reinoso, J. Rouquerol and K. S. Sing, *Pure Appl. Chem.*, 2015, **87**, 1051–1069.

81 (*a*) BRUKER AXS Inc., *APEX4, SAINT and SADABS*, Madison, WI, USA, 2021; (*b*) BRUKER AXS Inc., *XPREP – Reciprocal space exploration (Version 2014/2)*, Madison, WI, USA, 2014; (*c*) G. M. Sheldrick, *Acta Crystallogr., Sect. A:Found. Adv.*, 2015, **71**, 3–8; (*d*) G. M. Sheldrick, *Acta Crystallogr., Sect. C: Struct. Chem.*, 2015, **71**, 3–8; (*e*) C. B. Hübschle, G. M. Sheldrick and B. Dittrich, *J. Appl. Crystallogr.*, 2011, **44**, 1281–1284; (*f*) W. T. Pennington, *J. Appl. Crystallogr.*, 1999, **32**, 1028–1029; (*g*) A. L. Spek, *Acta Crystallogr., Sect. C: Struct. Chem.*, 2015, **71**, 9–18; (*h*) A. L. Spek, *Acta Crystallogr., Sect. E: Struct. Rep. Online*, 2020, **76**, 1–11; (*i*) A. L. Spek, *Inorg. Chim. Acta*, 2018, **470**, 232–237; (*j*) A. L. Spek, *Acta Crystallogr., Sect. D: Biol. Crystallogr.*, 2009, **65**, 148–155; (*k*) A. L. Spek, *J. Appl. Crystallogr.*, 2003, **36**, 7–13; (*l*) A. A. Coelho, *J. Appl. Crystallogr.*, 2018, **51**, 210–218; (*m*) M. S. Wrighton, D. S. Ginley and D. L. Morse, *J. Phys. Chem.*, 1974, **78**, 2229–2233; (*n*) A. E. Sedykh, M. Becker, M. T. Seuffert, D. Heuler, M. Maxeiner, D. G. Kurth, C. E. Housecroft, E. C. Constable and K. Müller-Buschbaum, *ChemPhotoChem*, 2023, **7**, e202200244; (*o*) F. Billes, H. Endrédi and G. Keresztury, *J. Mol. Struct.:THEOCHEM*, 2000, **530**, 183–200; (*p*) G. A. Foulds, G. C. Percy and D. A. Thornton, *Spectrochim. Acta, Part A*, 1978, **34**, 1231–1234; (*q*) K. I. Hadjiivanov, D. A. Panayotov, M. Y. Mihaylov, E. Z. Ivanova, K. K. Chakarova, S. M. Andonova and N. L. Drenchev, *Chem. Rev.*, 2021, **121**, 1286–1424; (*r*) C. S. Stan, P. Horlescu, M. Popa, A. Coroaba and L. E. Ursu, *New J. Chem.*, 2016, **40**, 6505–6512; (*s*) C. S. Stan, C. Peptu, N. Marcotte, P. Horlescu and D. Sutiman, *Inorg. Chim. Acta*, 2015, **429**, 160–167; (*t*) M. K. Trivedi and R. M. Tallapragada, *J. Mol. Pharm. Org. Process Res.*, 2015, **3**, 1000128; (*u*) K. B. Wiberg, V. A. Walters, K. N. Wong and S. D. Colson, *J. Phys. Chem.*, 1984, **88**, 6067–6075; (*v*) R. D. Shannon, *Acta Crystallogr., Sect. A*, 1976, **32**, 751–767; (*w*) R. Borjas Nevarez, S. M. Balasekaran, E. Kim, P. Weck and F. Poineau, *Acta Crystallogr., Sect. C: Struct. Chem.*, 2018, **74**, 307–311; (*x*) G. Bartlett and I. Langmuir, *J. Am. Chem. Soc.*, 1921, **43**, 84–91; (*y*) M. Topper, M. L. McLaughlin and F. R. Fronczek, *CSD Commun.*, 2007; (*z*) R. Balamurugan, M. Palaniandavar and R. S. Gopalan, *Inorg. Chem.*, 2001, **40**, 2246–2255; (*aa*) L. Jin, J. Ying, Y. Zhang, C. Sun, A. Tian and X. Wang, *New J. Chem.*, 2022, **46**, 8422–8432; (*ab*) R. Wartchow, *CSD Commun.*, 2019; (*ac*) D. Hass, O. Bechstein and M. Hentschel, *Z. Anorg. Allg. Chem.*, 1989, **576**, 131–138.